BRNO UNIVERSITY OF TECHNOLOGY

VYSOKÉ UČENÍ TECHNICKÉ V BRNĚ

FACULTY OF MECHANICAL ENGINEERING

FAKULTA STROJNÍHO INŽENÝRSTVÍ

INSTITUTE OF PHYSICAL ENGINEERING

ÚSTAV FYZIKÁLNÍHO INŽENÝRSTVÍ

PHASE PLATES FOR TRANSMISSION ELECTRON MICROSCOPY

FÁZOVÉ DESTIČKY PRO TRANSMISNÍ ELEKTRONOVOU MIKROSKOPII

MASTER'S THESIS

DIPLOMOVÁ PRÁCE

AUTHOR AUTOR PRÁCE	TEREZA ŠPIČÁKOVÁ
SUPERVISOR VEDOUCÍ PRÁCE	Ing. ANDREA KONEČNÁ, Ph.D.

BRNO 2022

BRNO UNIVERSITY OF TECHNOLOGY
FACULTY OF MECHANICAL ENGINEERING

Assignment Master's Thesis

Institut:	Institute of Physical Engineering
Student:	**Bc. Tereza Špičáková**
Degree programm:	Physical Engineering and Nanotechnology
Branch:	no specialisation
Supervisor:	**Ing. Andrea Konečná, Ph.D.**
Academic year:	2021/22

As provided for by the Act No. 111/98 Coll. on higher education institutions and the BUT Study and Examination Regulations, the director of the Institute hereby assigns the following topic of Master's Thesis:

Phase plates for transmission electron microscopy

Brief Description:

Transmission electron microscopy (TEM) provides an unprecedented spatial resolution that is key in understanding the structure of both inorganic and organic materials at the atomic scale. However, imaging samples consisting of light elements is often problematic due to weak contrast, which can be overcome by using phase plates introducing phase contrast. In addition, phase plates can be used to correct for aberrations of electron optics, or for generating on–demand special beam shapes.

In this thesis, different types of phase plates for TEM will be reviewed. Their advantages and disadvantages with respect to facile implementation in the instrument and also resulting image (or another signal) quality will be discussed. The performance of a selected type of phase plate will be tested experimentally in a microscope.

Master's Thesis goals:

1. Review different types of phase plates for transmission electron microscopy.
2. Evaluate which phase plates are the most feasible for a selected application (e.g. imaging weak–contrast samples, aberration correction,...) and design practical implementation in a specific transmission electron microscope.
3. Try to perform proof of principle experiments with the implemented solution.

Recommended bibliography:

REIMER, L., KOHL, H. Transmission Electron Microscopy: Physics of Image Formation. New York: Springer-Verlag New York, 2008. ISBN 978-0-387-40093-8.

BEDNÁR, J. „Chladná" moderní elektronová mikroskopie. Pokroky matematiky, fyziky a astronomie, 62 (2017), 237-253.

DANEV, R., BUIJSSE, B., KHOSHOUEI, M., PLITZKO, J. M., BAUMEISTER, W. Volta potential phase plate for in-focus phase contrast transmission electron microscopy. PNAS, 111 (2014), 15635-15640.

MALAC, M., HETTLER, S., HAYASHIDA, M., KANO, E., EGERTON, R. F., BELEGGIA, M.. Phase plates in the transmission electron microscope: operating principles and applications. Microscopy, 70 (2021), 75-115.

Deadline for submission Master's Thesis is given by the Schedule of the Academic year 2021/22

In Brno,

L. S.

prof. RNDr. Tomáš Šikola, CSc. Director of the Institute	doc. Ing. Jaroslav Katolický, Ph.D. FME dean

Summary

Samples consisting of light atoms, such as biological samples, provide low contrast in the transmission electron microscope images. However, introducing an additional phase shift between the electrons carrying the information of the sample and the background electrons can enhance the contrast significantly without impacting the quality of the image. This effect can be achieved by using a phase plate in the microscope. Phase plates based on a thin amorphous carbon film are used in conventional transmission electron microscopes. In recent years, extensive research in advanced phase plate design has been carried out. Yet, only a few studies on materials for the thin film-based phase plates have been published. For this reason, the main goal of this master's project is to design measurements of the phase-shifting properties of various materials.

In the first part of this thesis, the theory of electron wave imaging in a transmission electron microscope is described. Then, we review and compare phase plate designs. In the second part, four designs of the experimental setup are presented, out of which two have been tested experimentally. The measurements have been performed on a series of samples of different thicknesses and materials, and the results have been appropriately analysed. Furthermore, the qualitative behaviour of the tested designs has been compared to theoretical computations.

Abstrakt

Vzorky tvořené atomy lehčích prvků, jako jsou například biologické preparáty, dosahují na snímcích z transmisních elektronových mikroskopů nízkého kontrastu. Pokud však vneseme mezi elektrony nesoucí informaci o zkoumaném vzorku a elektrony pozadí dodatečný fázový posun, dojde k výraznému navýšení kontrastu bez negativních dopadů na kvalitu obrazu. Tohoto efektu lze v mikroskopech dosáhnout s pomocí fázových destiček. V konvenčních transmisních elektronových mikroskopech se běžně využívají fázové destičky založené na tenkých vrstvách amorfního uhlíku. V posledních letech byly detailně zkoumány různé pokročilé designy fázových destiček. Jen několik málo studií se však věnuje alternativním materiálům, které by bylo možné použít jako tenkovrstvé fázové destičky. Hlavním cílem této diplomové práce je tedy navrhnout způsoby měření fázových vlastností různých materiálů.

V první části práce je nejprve popsána teorie zobrazování elektronovou vlnou v transmisních elektronových mikroskopech. Dále jsou zde prezentovány a porovnány různé druhy fázových destiček. Ve druhé části práce jsou představeny čtyři návrhy experimentálního uspořádání, z nichž dva byly experimentálně otestovány. Tato měření byla provedena na sadách vzorků různých materiálů a tlouštěk a vhodně zpracována. Na závěr bylo kvalitativní chování těchto návrhů porovnáno s teoretickými výpočty.

Keywords

Transmission electron microscopy, phase plates, phase contrast, electron holography, electron diffraction

Klíčová slova

Transmisní elektronová mikroskopie, fázové destičky, fázový kontrast, elektronová holografie, difrakce elektronů

ŠPIČÁKOVÁ, T. *Phase plates for transmission electron microscopy.* Brno University of Technology, Faculty of Mechanical Engineering, 2022. 69 pg. Supervisor Ing. Andrea Konečná, Ph.D.

I declare that I have written my Master's Thesis on the theme of Phase plates for transmission electron microscopy independently, under the guidance of the supervisor Ing. Andrea Konečná, Ph.D., and using the sources quoted in the list of literature at the end of the Thesis.

Tereza Špičáková

First and foremost, I would like to express my undying gratitude that I was able to work on this thesis with the stellar duo of Andrea Konečná and Jan Jiša. Both of them have been a great support to me throughout and have guided this thesis to a successful conclusion with their boundless ideas, knowledge, enthusiasm, and also critical comments. Thank you for your friendly and supportive attitude. I very much appreciate the opportunity to have met and worked with you. I wish you nothing but the best and hope that we will stay in touch both professionally and personally.

Special thanks go to my classmate Martin Kulič, who performed comprehensive proofreading of the text and helped me solve some problems related to the work.

The work gradually moved towards a successful conclusion also thanks to the kindness and help of many of my colleagues at Thermo Fisher Scientific. I am grateful to Tomáš Brzobohatý, Jan Staníček, Petr Malek and Pavel Marák for their help in preparing the experimental setup. I also thank Lukáš Kachtik and Jaroslav Maniš for help with instrument training, Jan Hajduček for cosultations of the experiment and last but not least Petr Walek, Tom Meduňa and Hung Ngo Quang for help with programming and image processing. I would also like to thank my manager Jakub Chaloupka for his support during the work.

A great deal of gratitude goes then to all who created a pleasant, friendly environment while working on this thesis. I am mainly thinking of my dear colleagues in the office and selected first- and third-year Physical Engineering students. However, I would also like to thank everyone else, my classmates, friends, and especially my family, for the bottomless support they provide me. Last but not least, I would like to express my gratitude to the teachers and students of Physical Engineering for co-creating such an enjoyable and inspiring environment during the studies that will forever remain in my heart.

This thesis would not have been possible without the contribution of Thermo Fisher Scientific company, which allowed me to work on this thesis as part of my internship, provided all the equipment, and funded the thesis. Thanks for this opportunity, which I greatly appreciate.

Tereza Špičáková

Contents

Introduction 3

1 Transmission electron microscopy 5

1.1 Electron wave optics 6

1.1.1 Wave function of a particle 6

1.1.2 Introduction to wave optics 10

1.2 Image formation in a TEM 12

1.2.1 Electron-sample interaction 12

1.2.2 Contrast in a TEM 15

1.3 Imaging system of a TEM 17

1.3.1 Magnetic lenses 19

1.3.2 TEM optical system 22

1.4 Phase plates 24

1.4.1 Contrast transfer function 25

1.4.2 Thin film phase plates 26

1.4.3 Electrostatic phase plates 28

1.4.4 Magnetic phase plates 29

1.4.5 Phase plates comparison 30

2 Phase plate implementation 33

2.1 Phase shift measurement designs 33

2.1.1 Electron biprism 33

2.1.2 Diffraction grid beam splitting 35

2.1.3 Defocused edge image 39

2.2 Phase plate effect simulations 39

2.2.1 Diffraction grid simulation 40
2.2.2 Defocused edge simulation 41
2.3 Experimental setup preparations 43
2.3.1 Phase plate test samples 43
2.3.2 Diffraction grid 44
2.4 Phase shift measurement 47
2.4.1 Diffraction grid measurement 47
2.4.2 Defocused edge measurement 52

Conclusions **59**

Bibliography **61**

List of Abbreviations **68**

List of Supplementary Material **69**

Introduction

In the nineteenth century, a German physicist Ernst Karl Abbe discovered the diffraction limit which states that the highest resolution achievable in an optical system is determined by the wavelength of the light used and by the numerical aperture of the projection system. As no further information from the image can be achieved when magnifying an image at the resolution limit, the height of the imaging technique seemed to be reached. Shortly after, a French quantum physicist Louis de Broglie introduced his theory in which wave properties were assigned to particles. The wave-particle dualism theory for which he was awarded with a Nobel Prize launched a completely new era of both physics and technology.

A German physicist Ernst Ruska realized the significance of the theory and only few years later, in 1933, he constructed the first electron microscope. Although the device suffered from many aberrations and the obtained images were of worse quality than those of conventional light-optical microscopes, he proof of concept they made meant a revolution within the imaging techniques. For this invention, Ernst Ruska received a Nobel Prize in 1986.

Since then, the field of electron optics has experienced a great and fast development. Invention of new imaging techniques and high technology implementation into the microscopes have moved the resolution to sub-Angstroem values [1, 2]. Moreover, taking advantage of modern computers, large data can be stored and processed leading to additional information achievable from the electron microscope images. All of these discoveries have brought modern science to the point where individual atoms can be observed [3], finding its use in material science, semiconductor technology and biological studies among other fields of interest.

The application of the electron microscopy within life science has been however challenging since the need of vacuum in the microscopes led to destruction of the samples caused by rapid water evaporation. The solution to this problem was introduced in the early eighties of the last century by Jacques Dubochet and his collaborants arriving to so-called cryo-electron microscopy. This technique is based on rapid cooling of the samples in liquid nitrogen, which results in formation of an amorphous water ice instead of its common crystalline form, completely avoiding the issue of structural damage to the samples. In this way, a high-resolution biomolecule observation became possible, leading to new discoveries in the field of life science as well as another Nobel Prize for the electron microscopes development given to Dubochet and his collegues Joachim Frank and Richard Henderson in 2017.

However, one major issue with observing biological specimens still remains. Since very low scattering occurs on biological samples, the electron microscope images of those

samples provide very low contrast. This issue can be overcome by using phase plates - simple devices introducing a phase shift to an electron wave passing through them. So far, many different concepts of phase plates have been introduced. The main focus of this thesis is an overview and comparison of these designs, along with designs of possible implementations of phase plates in modern conventional transmission electron microscopes. Part of this work is also devoted to measurements of phase plates properties.

Chapter 1

Transmission electron microscopy

In a conventional transmission electron microscope (TEM), a sample is irradiated by a 100-400 keV uniform electron beam. The transmitted electrons carry information about the sample and form image that we observe and analyze. As will be delivered later, the higher the energy of an electron, the shorter the wavelength. A 200 keV electron beam reaches a wavelength of approximately 2.5 pm, which is more than five orders of magnitude less then the wavelength of visible light. According to the Rayleigh's diffraction limit, the achievable resolution δ is determined by the wavelength λ, the incident angle α and the refractive index n of the surrounding media as $\delta = \frac{0.61\lambda}{n \sin\theta}$. Hence, the resolution of a TEM should be able to reach tens of pm. However, due to extensive aberrations of the microscope optical system, the resolution of most modern TEMs is limited to several nanometers. In the most high-end aberration-corrected microscopes, a sub-angstroem resolution has been reached [1, 2].

The electrons are emitted from an electron gun and accelerated by a group of electrodes of gradually increasing voltages. The electron beam is then formed by a system of magnetic lenses and an image of the specimen is projected onto a fluorescent screen or a CCD camera. As the electron beam can get easily scattered by larger particles, high vacuum has to be maintained along the electron path. Moreover, vibration dampers and electromagnetic shielding are usually present in order to prevent any unwanted curvature of the beam which would have negative effects on the image quality.

The application of TEMs consists of three main research and industrial fields. In material science, these microscopes are used to analyze material and crystallographic structure of a sample as well as the defects present in the sample at an atomic scale. TEMs equipped with a cryo-electron microscopy extension are used within life science research to study proteins, viruses, lipid molecules, etc. [4]. Within the industrial applications, the semiconductor sector is the most remarkable purchaser of the TEMs as the quality of modern electronic structures manufacturing can only be inspected with those microscopes.

A detailed description of all the principles and functioning elements of a TEM is far beyond the scope of this thesis. Complex books dedicated to those devices have been published by great authorities in the field of transmission electron microscopy [5, 6, 7]. In the following sections, we will focus on electron wave imaging, from a fundamental electron wave function derivation to a constructional solution of a TEM optical system. If

unspecified, the information in those sections comes either from the transmission electron microscopy books mentioned [5, 6, 7] or from a general knowledge gained either in several courses or in practice.

1.1. Electron wave optics

1.1.1. Wave function of a particle

In 1924, Louis de Broglie published his theory that free particles (particles that no force acts on) might be described as monochromatic plane waves propagating in time t and space $\vec{r}$

$$\psi(\vec{r},\ t) = \psi_0 \exp(\mathrm{i}(\vec{k} \cdot \vec{r} - \omega t)), \tag{1.1}$$

where $\vec{k}$ is the wave vector related to the wavelength by $\lambda = 2\pi/|\vec{k}|$ and ω is the angular frequency. By this statement, he reacted to Albert Einstein's hypothesis that electromagnetic waves propagate in quanta and thus can act as particles. The particle energy E and momentum $\vec{p}$ can then be linked to the wave properties using relations

$$E = \hbar\omega \tag{1.2}$$

and

$$\vec{p} = \hbar\vec{k}, \tag{1.3}$$

where $\hbar = h/2\pi$ is the reduced Planck constant [8].

Erwin Schrödinger further developed this theory, stating that any moving particle can be described by its wave function. Although the wave function doesn't have a physical significance, the square of modulus of this function $|\psi(\vec{r},t)|^2 = \psi(\vec{r},t)\psi^*(\vec{r},t)$ does, describing the probability density of detecting the particle at time t in position $\vec{r}$. Schrödinger also discovered a differential equation describing the time evolution of such a wave function of a particle moving in a potential field. This equation, known as the Schrödinger equation, is a fundamental equation of quantum mechanics, stating that

$$\mathrm{i}\hbar\frac{\partial\psi(\vec{r},t)}{\partial t} = \hat{H}\psi, \tag{1.4}$$

where $\hat{H}$ is called the Hamiltonian and it is the total energy operator. If the potential fields acting on the particle are time-independent, the Schrödinger equation might be solved by variable separation. Assuming separability of the wave function and assigning $\psi(\vec{r},t) = f(t)\varphi(\vec{r})$, one finds

$$f(t) = \mathrm{e}^{-\mathrm{i}\frac{E}{\hbar}t}$$

and

$$\hat{H}\varphi(\vec{r}) = E\varphi(\vec{r}). \tag{1.5}$$

Here, the constant E is an eigenvalue of the Hamilton operator and it can be interpreted as the total energy of the particle. The function $\varphi(\vec{r})$ is thus an eigenfunction of the operator. The latter equation represents the so called stationary Schrödinger equation.

Relativistic correction

For electrons, non-relativistic relations can be used to approximate their behavior for acceleration voltages below 40 keV [7]. However, since the acceleration voltages in conventional TEMs reach hundreds of keV, relativistic correction needs to be taken into account. The energy of a relativistic electron with rest mass m_0 accelerated by the potential U is given by

$$E = mc^2 = m_0c^2 + eU.$$

In the former relation, c is the speed of light and m is the relativistic mass related to the rest mass as $m = \gamma m_0$, where

$$\gamma = \left(1 - \frac{v^2}{c^2}\right)^{-1/2}$$

is known as the Lorentz factor. As for $v \ll c$ the electron energy is only given by $m_0c^2 \equiv E_0$, this term is called the rest energy of the electron. The other term $eU \equiv E$ corresponds to the kinetic energy of the electron in the non-relativistic limit. Therefore, the Lorentz factor can be then also approximated as $\gamma \approx 1 + E/E_0$.

In the non-relativistic approach, the total energy of a free particle used in the stationary Schrödinger equation (1.5) is given by the kinetic energy $E = eU$. As derived in [5], the relativistically corrected total energy can be expressed as

$$\mathcal{E} = E\frac{2E_0 + E}{2(E_0 + E)}. \tag{1.6}$$

For small energies $E \ll E_0$, this relation converges to the non-relativistic approach limit. The relativistically corrected stationary Schrödinger equation thus gives

$$\hat{H}\varphi(\vec{r}) = \mathcal{E}\varphi(\vec{r}) = E\frac{2E_0 + E}{2(E_0 + E)}\varphi(\vec{r}). \tag{1.7}$$

WKB approximation

In the following, an approximate solution of the stationary Schrödinger equation will be derived using so-called WKB approximation [9, 10]. Let's consider a particle of relativistic mass m moving in a stationary force potential $V(\vec{r})$ with momentum $\vec{p}$. The Hamilton operator can be then expressed as $\hat{H}(\vec{r}) = \frac{\hat{\vec{p}}^2}{2m} + V(\vec{r})$, where $\hat{\vec{p}}$ is the momentum operator. As the momentum of a particle generates its translation through space, the momentum operator in the coordinate representation can be expressed as $\hat{\vec{p}} = \mathrm{i}\hbar\vec{\nabla} = \mathrm{i}\hbar\left(\frac{\partial}{\partial x}, \frac{\partial}{\partial y}, \frac{\partial}{\partial z}\right)$. The resulting form of the stationary Schrödinger equation is then

$$\left[-\frac{\hbar^2}{2m}\vec{\nabla}^2 + V(\vec{r})\right]\varphi(\vec{r}) = \mathcal{E}\varphi(\vec{r}).$$

In the case of a one-dimensional problem or a three-dimensional radially symmetric problem, the solution of this equation might be considered in the form of $\varphi = A(\vec{r})\mathrm{e}^{\mathrm{i}\phi(\vec{r})}$, where $A(\vec{r})$ and $\phi(\vec{r})$ are real functions [11]. Substituting this form into the the latter equation leads to

$$-\frac{\hbar^2}{2m}\left[\vec{\nabla}^2 A + 2\mathrm{i}\vec{\nabla}A\vec{\nabla}\phi + \mathrm{i}A\vec{\nabla}^2\phi - A\left(\vec{\nabla}\phi\right)^2 + VA\right] = \mathcal{E}A.$$

As all the functions are real, we can split the equation into its real and imaginary parts. Using $\vec{\nabla}(A^2\vec{\nabla}\phi) = A(2A\vec{\nabla}A\vec{\nabla}\phi + A\vec{\nabla}^2\phi)$, the solution of the imaginary part of the equation above can be written as

$$A = C/\sqrt{\vec{\nabla}\phi},$$

where C is a constant and the real part of the equation yields to

$$\frac{\hbar^2}{2m}\left[\vec{\nabla}^2 A - A\left(\vec{\nabla}^2\phi\right)\right] + (\mathcal{E} - V)A = 0.$$

The WKB approximation, named after physicists Gregor Wentzel, Hendrik Anthony Kramers, and Léon Brillouin, is a method to estimate the solution of a linear second-order differential equation with spatially varying coefficients. In this approximation, the highest derivative of a variable in the equation can be neglected with respect to the other terms when multiplied by a small constant parameter. In the case of the Schrödinger equation, we thus neglect the term $\vec{\nabla}^2 A$ when the condition $\frac{\hbar^2}{2m}\vec{\nabla}^2 A \ll (\mathcal{E} - V)A$ is fulfilled. The relative phase of the wave function of the particle moving from $\vec{r_0}$ to $\vec{r}$ is then given by

$$\phi(\vec{r}) = \pm \int_{\vec{r_0}}^{\vec{r}} \frac{\sqrt{2m(\mathcal{E} - V(\vec{r'}))}}{\hbar} \mathrm{d}\vec{r'}. \tag{1.8}$$

Substituting $\vec{k}^2(\vec{r}) \equiv \frac{2m}{\hbar^2}(\mathcal{E} - V(\vec{r}))$, where the vector $\vec{k}$ points parallel to the momentum $\vec{p}$ particle, we find that the wave function of the particle is given by

$$\psi(\vec{r}, t) = \left\{ \frac{C_+}{\sqrt{k(\vec{r})}} \mathrm{e}^{\mathrm{i}\int_{\vec{r_0}}^{\vec{r}} \vec{k}(\vec{r'})\cdot \mathrm{d}\vec{r'}} + \frac{C_-}{\sqrt{k(\vec{r})}} \mathrm{e}^{-\mathrm{i}\int_{\vec{r_0}}^{\vec{r}} \vec{k}(\vec{r'})\cdot \mathrm{d}\vec{r'}} \right\} \mathrm{e}^{-\mathrm{i}\frac{\mathcal{E}}{\hbar}t}, \tag{1.9}$$

where C_+ and C_- are constants. It can be shown that the vector $\vec{k}$ is related to the particle momentum as (1.3). Thus, $\vec{k}$ can be interpreted as a local wave vector of the particle, and we can define local wavelength of the particle as $\lambda(\vec{r}) = 2\pi/|\vec{k}| = h/\sqrt{2m(\mathcal{E} - V(\vec{r}))}$. Notice that in the case of a constant potential V, the wave function reduces into the superposition of two de Broglie's plane waves introduced in (1.1) propagating in opposite directions.

Charged particle in an electromagnetic field

In the terms of classical physics, a charged particle moving in an electric field $\vec{E}$ and magnetic field $\vec{B}$ with velocity $\vec{v}$ is influenced by those fields via Lorentz force

$$\vec{F} = q\left(\vec{E} + \vec{v} \times \vec{B}\right),$$

where q is the charge of the particle. The fields can be described using scalar potential U and vector potential $\vec{A}$ as

$$\vec{E} = -\vec{\nabla}U - \frac{\partial \vec{A}}{\partial t}, \tag{1.10}$$

$$\vec{B} = \vec{\nabla} \times \vec{A}. \tag{1.11}$$

In the case of time-independent fields, we can use the scalar and vector potential separately to describe the effect of electric and magnetic field, respectively.

The quantum effect of the electromagnetic field is fully described by the Hamilton operator

$$\hat{H}(\vec{r},t) = \frac{1}{2m}\left(\vec{p} - q\vec{A}(\vec{r},t)\right)^2 + qU(\vec{r},t), \tag{1.12}$$

where m is the mass of the particle moving in this field. In the absence of a magnetic field, the operator reduces to the form discussed in previous section. Here, the operator of potential energy $V(\vec{r})$ is related to the electrostatic potential $U(\vec{r})$ as $V(\vec{r}) = qU(\vec{r})$. The wave function of the particle affected by this field then follows (1.9).

In the case of presence of a magnetic field, the term $\vec{p} - q\vec{A}(\vec{r},t)$ can be considered as a generalized momentum operator [9]. Substituting $\vec{k} = \left(\vec{p} - q\vec{A}(\vec{r},t)\right)/\hbar$ in (1.9), we get the phase of the wave function as

$$\phi(\vec{r}) = \int_{\vec{r_0}}^{\vec{r}} \left(\vec{p} - q\vec{A}(\vec{r},t)\right) \cdot \mathrm{d}\vec{r}.$$

As will be discussed later, the phase is not a measurable quantity. However, the phase difference between two wave functions is.

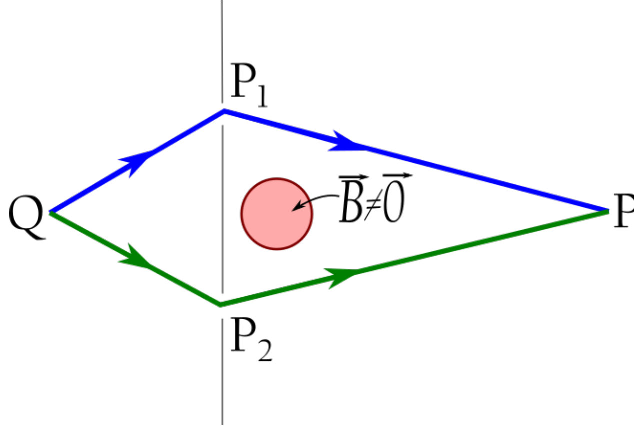

Figure 1.1: Aharonov Bohm effect. Magnetic field traversing the red area enclosed by a pair of electron trajectories induces a phase shift between the electrons moving along those trajectories. Taken and adapted from [5].

Let us now consider the situation shown in Figure 1.1. Two electron waves originate from a source at point Q and have identical properties at this point. Each of them passes through one of the two slits S1 and S2 and they meet again at point P behind the slits. The phase difference between the two waves is given by

$$\begin{aligned} \phi_2 - \phi_1 &= 2\pi\left(\int_Q^{S_2} \vec{k}\cdot \mathrm{d}\vec{r} + \int_{S_2}^{P} \vec{k}\cdot \mathrm{d}r - \int_Q^{S_1} \vec{k}\cdot \mathrm{d}\vec{r} - \int_{S_1}^{P} \vec{k}\cdot \mathrm{d}r\right) \\ &= \frac{2\pi}{h}\oint_c (\vec{p} - q\vec{A})\cdot \mathrm{d}\vec{r}, \end{aligned}$$

where the four integrals are reduced into an integral over closed loop $c = QS_1PS_2Q$. Applying the Stoke's law and the relation (1.11) to the integral involving $\vec{A}$, we get

$$\begin{aligned}\phi_2 - \phi_1 &= \frac{2\pi}{h}\oint_c \vec{p}\cdot \mathrm{d}\vec{r} - \frac{2\pi q}{h}\int_S \vec{B}\cdot \mathrm{d}\vec{S'} \\ &\equiv \frac{2\pi}{h}\oint_c \vec{p}\cdot \mathrm{d}\vec{r} - \frac{2\pi q}{h}\Phi_\mathrm{m}.\end{aligned}$$

The effect of the magnetic field on the phase difference of the two waves is thus expressed in the terms of magnetic flux Φ_m passing through the loop of the two trajectories. This is called Aharonov-Bohm effect. It is interesting to note that the phase shift induced by the magnetic flux occurs even when there is no magnetic field on the trajectories that would act on the particles in the terms of Lorentz force.

1.1.2. Introduction to wave optics

The propagation of an electron wave can be described as propagation of a wavefront, which is a continuous area of the wave having the same phase. According to the Huygens-Fresnel principle, each surface element $\mathrm{d}S$ of the wavefront $\psi(x_0, y_0, z_0)$ generates a secondary spherical wave

$$\mathrm{d}\psi(x,y,z) = \psi(x_0,y_0,z_0)\frac{A(\theta)}{2\mathrm{i}\lambda}\frac{\mathrm{e}^{\mathrm{i}kr}}{r}\mathrm{d}S,$$

where $k = 2\pi/\lambda$ is the wave vector, r denotes the magnitude of the translation vector $\vec{r} = (x - x_0, y - y_0, z - z_0)$, $A(\theta) = 1 + \cos\theta$ is the so-called inclination factor and θ is the angle of emission to the normal of the wavefront [5]. As discussed in [12], the exact form of the inclination factor is not crucial for the for the calculations and it will be thus neglected in the further considerations. A new wavefront is then given by the superposition of those elemental spherical waves $\psi = \int \mathrm{d}\psi$.

Let's consider a coordinate system with z going parallel to the optical axis. In the paraxial approximation, hence for small propagation angles

$$\alpha = \sqrt{(x-x_0)^2 + (y-y_0)^2}/(z-z_0) \ll 1,$$

the distance r can be rewritten as $r \approx z + \frac{(x-x_0)^2+(y-y_0)^2}{2(z-z_0)}$ and the reciprocal value of r can be further simplified as $1/r \approx 1/(z - z_0)$. Moreover, the wavefront in the paraxial approximation can be considered to be perpendicular to the z axis. Thus, the relation for a propagating wave can be approximated as

$$\psi(x,y,z) = \frac{1}{2\mathrm{i}\lambda}\frac{\mathrm{e}^{\mathrm{i}k(z-z_0)}}{z-z_0}\iint_{-\infty}^{\infty}\psi(x_0,y_0,z_0)\mathrm{e}^{\mathrm{i}k\left[(x-x_0)^2+(y-y_0)^2\right]/2(z-z_0)}\mathrm{d}x_0\mathrm{d}y_0. \quad (1.13)$$

Expanding the exponential term in the integral and substituting $kx/\pi \equiv q_x$, $ky/\pi \equiv q_y$, we find out that the propagation of the wave can be expressed in the terms of Fourier transform $\mathcal{F}\{f(x,y)\}(q_x,q_y) = \iint_{-\infty}^{\infty} f(x,y)\mathrm{e}^{2\pi\mathrm{i}(xq_x+yq_y)}$

$$\psi(x,y,z) = \frac{1}{2\mathrm{i}\lambda}\frac{\mathrm{e}^{\mathrm{i}k(z-z_0)}}{z-z_0}\mathrm{e}^{\mathrm{i}k(x^2+y^2)/2(z-z_0)}\mathcal{F}\left\{\psi(x_0,y_0,z_0)\mathrm{e}^{\mathrm{i}k(x_0^2+y_0^2)/2(z-z_0)}\right\}.$$

Imaging with a lens

A perfect thin lens focuses a parallel beam to a single point on the optical axes in distance f from the lens. In the paraxial approximation, this can be described in the terms of a phase factor ϕ_f depending on the distance from the optical axis

$$\phi_\mathrm{f}(x, y) = \mathrm{e}^{-\mathrm{i}k(x^2+y^2)/2f}, \tag{1.14}$$

where f is called the focal length of the lens. Please note that the sign in the argument of the exponential function is opposite to the sign used in the propagation formula. Generally, the focal length can be both positive and negative. Thus, we can distinguish convex lenses with $f > 0$ and concave lenses with $f < 0$.

In order to describe the imaging effect of a lens, a sign convention needs to be established. In the following text, the z position of an object will be considered positive when it is placed in front of the lens. On the other hand, the position z of the image will be considered positive when the image is created behind the lens (see Figure 1.2). As the orientation of both the object and the image will not be crucial in the thesis, only absolute size $h \equiv \sqrt{x^2 + y^2}$ of both will be considered.

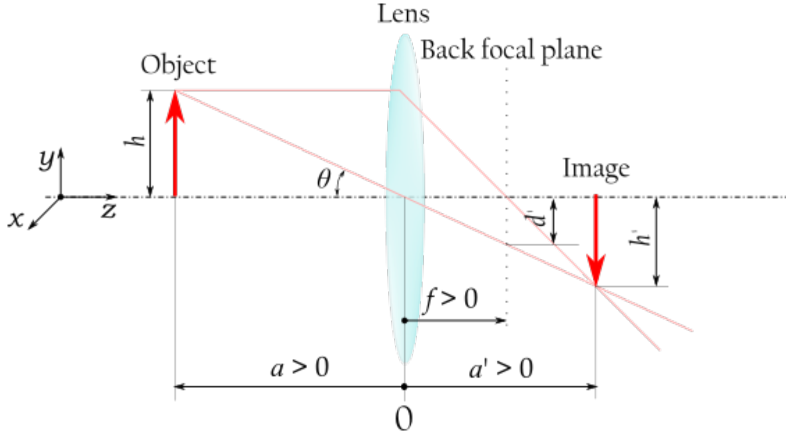

Figure 1.2: Sign convention for imaging with a lens.

A point source at a position $z = a$, $\sqrt{x^2 + y^2} = h$ in front of a lens is focused to another single point at the position $z = a'$, $\sqrt{x^2 + y^2} = h'$. The ratio between the size of the object and its image

$$M = \left|\frac{a'}{a}\right| = \frac{h'}{h} \tag{1.15}$$

is called the magnification. The relation between the positions of the object and the image can be described by the thin lens formula

$$\frac{1}{a} + \frac{1}{a'} = \frac{1}{f}. \tag{1.16}$$

The validity of the latter equation can be verified using the propagation operator (1.1.2). The wave function in the image plane can be derived by propagating the wave from the sample onto a lens, applying the lens operator (1.14) and propagating the resulting wave to the image plane determined by (1.16). Simplifying the resulting wave function, one can

find out that the result is proportional to the original wave function in the sample plane. Similarly, the wave function in the back focal plane of the lens can be derived. As shown in [12], the wave function in this plane corresponds to the Fourier transform of the wave function in the sample plane $\mathcal{F}\{\psi\}$. The information obtained in this plane contains the projection of the reciprocal space. As the coordinates in the back focal plane correspond to the propagation directions of the original beams, diffraction properties of the sample can be thus analyzed there. The image in this plane is called the diffractogram.

1.2. Image formation in a TEM

1.2.1. Electron-sample interaction

The highly energetic electrons traverse a specimen and interact with it, specifically its atoms' nuclei and the bound electrons and free electrons of the specimen. As a result of this interaction, the electrons might deflect from their original direction and in the case of inelastic scattering, they also lose part of their energy. Both elastically (when the energy is conserved) and inelastically scattered electrons carry an information about the specimen. In a standard TEM mode, an objective aperture is used to trap electrons scattered by angles typically higher than 30 mrad. The remaining electrons then go down through the imaging system of the microscope and create an image of the sample.

In the particle approach, the scattering can be described in the terms of scattering cross-section $\frac{\mathrm{d}\sigma}{\mathrm{d}\Omega}$. It is a probability of scattering of a single electron $\mathrm{d}\sigma$ passing e.g. on an atomic potential into a cone of solid angle $\mathrm{d}\Omega$, making an angle of θ with respect to the original direction of the electron's motion. The total scattering-cross section is then obtained by integrating the term $\frac{\mathrm{d}\sigma}{\mathrm{d}\Omega}$ over the solid angle. Considering a geometrical relationship $\Omega = 2\pi(1-\cos\theta)$, we write

$$\sigma_{\mathrm{t}} = \int_0^{\pi} \frac{\mathrm{d}\sigma}{\mathrm{d}\Omega} 2\pi \sin\theta \mathrm{d}\theta.$$

When multiple atoms are present along the electron's trajectory, the probability of the scattering increases. As derived in [5], for a sample of atomic density N and a thickness x and an incident electron beam of n_0 particles, the amount of unscattered electrons n is given by

$$n = n_0 \exp\left(-N\sigma_{\mathrm{t}}x\right) = n_0 \exp\left(-x/x_{\mathrm{t}}\right). \tag{1.17}$$

The quantity $x_{\mathrm{t}} \equiv 1/(N\sigma_{\mathrm{t}})$ is known as the total mean free path and it corresponds to a path length of an electron passing through a specimen with the scattering probability 1/e. For conventional materials and an electron beam with energy of 200 kV, the mean free path is in the order of tens to hundreds of nanometers [13, 14]. When the sample width exceeds few hundred nanometers, most of the electrons get scattered on the sample and the transmission signal decreases. Therefore, most of the conventional TEM samples are tens of nanometers thick.

As mentioned above, we distinguish elastic and inelastic scattering events, though the formalism presented above can be applied to both of those mechanisms. The scattering

cross-section is then a sum of the cross-sections of the elastic and inelastic scattering σ_{el} and σ_{inel} respectively. However, there is a significant difference between both scattering mechanisms including the effect on the image creation. In the following chapters, both mechanisms will be discussed in more detail.

Elastic scattering

When electrons pass through a specimen, they experience a potential field of the charged particles within the sample. The atom's nuclei create a positive potential distribution shielded by the field of the atomic electrons. A negatively charged electron experiences this field and gets attracted by the positive potential. Consequently, it can get deflected from its original direction, i.e. scattered as shown in Figure 1.3. As the atomic spacing is large with respect to the size of the nuclei, most of the electrons experience only weak, shielded electric field and thus scatter by low angles. The deeper an electron penetrates into the electron cloud of an atom, the more it gets scattered. In the limiting case, the electron can undergo so called back-scattering, where the scattering angle exceeds 90°.

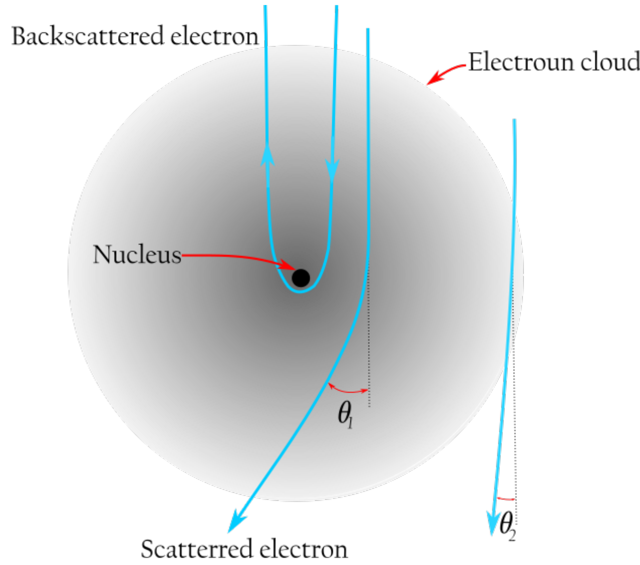

Figure 1.3: Elastic scattering of an electron (blue) from the spatial charge of an atom. Taken and adapted from [6].

High-angle elastic electron scattering was first described by Ernest Rutherford [6] who also derived an analytical expression for the electron-nucleus scattering cross-section. This expression has been further modified in order to include the effect of the electron cloud shielding and relativistic effects. The resulting formula follows [6]

$$\sigma_{\mathrm{R}}(\theta) = \frac{Z^2 \lambda_{\mathrm{R}}^4}{64\pi^4 a_0^2} \frac{d\Omega}{\left[\sin^2\left(\frac{\theta}{2}\right) + \frac{\theta_0^2}{4}\right]^2}.$$

Here Z is the atomic number, a_0 is the Bohr radius, λ_{R} is the relativistically corrected electron wavelength, and θ_0 is the so-called screening parameter defined by the atomic number and the electron energy. Although this formula is only valid for electron beam

energies below 300 keV and atomic numbers below 30, it is widely used for calculations in transmission electron microscopy.

The scattering-cross section approach is convenient as it gives a good estimate of the scattering process. In some applications, however, it is not sufficient as it does not involve the wave properties of electrons. Another approach used in context of elastic scattering is relying on the atomic-scattering factor $f(\theta)$ which describes the effect of the scattering on the electron wave amplitude. It is related to the elastic scattering cross-section as $|f(\theta)|^2 = \frac{d\sigma}{d\Omega}$. The relationship between the atomic-scattering factor and the electric potential distribution $U(r)$ in the sample is given by

$$f(\theta) \propto \int_0^\infty r^2 U(r) \frac{\sin(4\pi \sin(\theta/\lambda) r)}{4\pi \sin(\theta/\lambda) r} \mathrm{d}r.$$

As shown in section 1.1.1, the potential distribution also has an effect on the phase of the electrons. Assuming that the potential energy V of the electrons moving in this field is much smaller than their relativistically corrected kinetic energy $\mathcal{E}$, the integrand in equation (1.8) might be rewritten as $\frac{\sqrt{2m(\mathcal{E}-V(\vec{r}))}}{\hbar} \approx \frac{\sqrt{2m\mathcal{E}}}{\hbar}(1 - V(\vec{r})/\mathcal{E})$. The phase change of the electron wavefunction induced by the scattering event is thus approximately equal to

$$\Delta\phi(\vec{r})) \approx \frac{e}{\hbar}\sqrt{\frac{m}{2\mathcal{E}}} \int_{\vec{r_0}}^{\vec{r}} U(\vec{r'})\mathrm{d}\vec{r'}. \quad (1.18)$$

The effect of the specimen as whole is given by summation of the contributions of the individual atoms. When a specimen is much thicker than the interatomic distances, the effect of the sample on the electron wave can be described using so-called mean inner potential U_{mean}. The integral in (1.18) is then replaced by the value $U_{\mathrm{mean}}t$, where t is the thickness of the sample. The values of the mean inner potential of various materials can be then determined by measuring the phase shift of an electron wave passing through the material with respect to a reference wave passing through vacuum.

When the structure of the specimen is periodic, we find that scattering in specific directions is preferable. This results in a diffraction of the primary beam on the sample. As described in 1.1.2, the scattering angle is related to the spatial period of the sample Λ as $\sin\theta = n\lambda/\Lambda$, where λ is the electron wavelength and $n \in \mathbb{Z}$. Hence, the scattering angle of an electron corresponds to the spatial frequency $q = 2\pi/\Lambda$ the electron carries information of.

Inelastic scattering

During the inelastic scattering, part of the kinetic energy of the primary electrons is transferred to the specimen, enabling excited states of the specimen to occur. Those changes of primary beam energy can be observed using electron energy loss spectroscopy. Measuring the energy spectra in a scanning mode, we can obtain multidimensional sample images including the excitation maps. Using energy filters, we can then achieve both higher contrast images (when filtering out the inelastically scattered electrons) and images of the excitations induced by the primary beam (when using electrons with a specific energy loss only). However, as a result of the excitation and deexcitation processes,

secondary particles might also be generated and detected inside the microscope. The individual sources of signal are shown in Figure 1.4. Detailed description of the inelastic scattering mechanism is beyond the scope of this thesis, so only the most significant processes will be briefly discussed in the following paragraph.

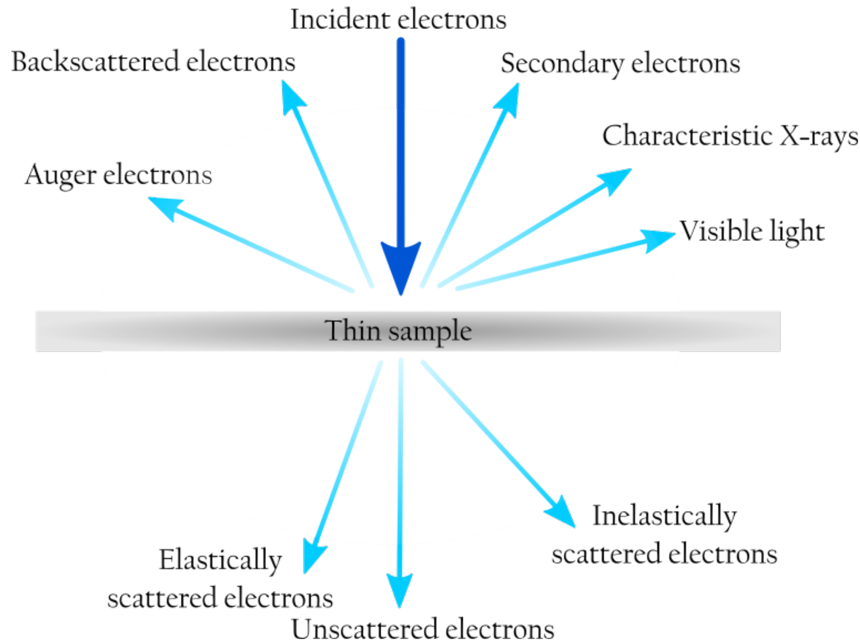

Figure 1.4: Particles creating a signal in a TEM. Taken and adapted from [6].

Most of the energy losses of the primary beam originate from the interaction with bound electrons of the sample. The primary beam can excite electrons to higher energy states within the electron shell or eject the electrons from the topmost energy levels and thus generate secondary electrons. In the case of the core electron excitations, the released energy state is filled by an electron from a higher level. The released energy is then radiated in the form of X-rays or used to eject a valence electron generating the signal of so-called Auger electrons. The primary beam can, however, also generate resonant collective oscillations of (nearly) free electrons, known as plasmons. Moreover, collective oscillations of the atoms arranged in a lattice, known as phonons, may occur. The secondary particle signal is usually used for chemical composition analysis with high spatial resolution. Taking the advantage of coincidence-detection techniques, the energy resolution of the spectra can be enhanced [15]. The possibility of plasmon detection is then significant in the field of nanophotonics and solid state physics [16]. The objective of this thesis is, however, imaging with the unscattered and elastically scattered electrons only. Thus, the inelastic scattering will be considered as a side effect and in most considerations, the effect will be neglected.

1.2.2. Contrast in a TEM

After the interaction with the sample, the electron beam carries information about the sample imprinted in both the amplitude and phase of the electron wave ψ. Using an imaging system described in more detail in the following section, an image of the specimen

can be formed. However, the detectors used in a microscope, not unlike the human eye, cannot observe the complex electron wave function and can only detect the intensity of the wave function given by

$$I = |\psi|^2 .$$

The measurable information of the specimen is then given by the variations of intensity. The quantity that describes the relative difference of intensities I_1 and I_2 is called contrast (C) and it is defined as

$$C = \left| \frac{I_2 - I_1}{I_2 + I_1} \right| .$$

The minimum contrast detectable by a human eye is in the range of 5 % and 10 % [7]. Although digital recording of the image enables us to enhance the contrast of the image using postprocessing methods, it is still desirable to obtain high enough contrast in the image in order to extract as much information about the sample as possible.

In a transmission electron microscope, two mechanisms of contrast generation can be distinguished – amplitude contrast (or scattering contrast in some literature) and phase contrast. Both types of the contrast contribute to the image simultaneously, although in many situations one of them dominates. In the following text, the mechanisms and significance of both types of contrast will be discussed.

Amplitude contrast

The amplitude (or scattering) contrast is based on high-angle elastic scattering of the electrons on the specimen. As discussed in section 1.1.2, in the back focal plane of the objective lens, the distribution of the electrons is determined by the angle of their trajectories with respect to the optical axis. The relationship between the angle of the trajectory θ and the distance from the optical axis r is given by $r = f\,\mathrm{tan}\theta \approx f\theta$ in the small angle limit, where f is the focal length of the objective lens. When an aperture of radius R is placed into this plane, electrons scattered by angle $\theta > R/f$ are intercepted by the aperture and thus do not contribute to the image. Consequently, the areas of the sample where electrons are more likely to scatter in higher angles are less intense in the image.

As shown in section 1.2.1, the scattering cross-section $\frac{\mathrm{d}\sigma}{\mathrm{d}\Omega}$ depends on the atomic number Z as $\frac{\mathrm{d}\sigma}{\mathrm{d}\Omega} \propto Z^2$. The number of electrons scattered by a specimen of thickness t is then given by $n = n_0 \exp(-N\sigma t)$, where n_0 is the total amount of electrons and N is the atomic density. Therefore, the areas of a specimen of the same thickness but different mass density, as well as areas of the same density but different thickness, will be imaged with different intensity, see Figure 1.5. The amplitude contrast is thus often called the mass contrast. This contrast mechanism is dominant for imaging samples for material science, where, among other uses, it enables localization of different material phases or dislocations in the specimen.

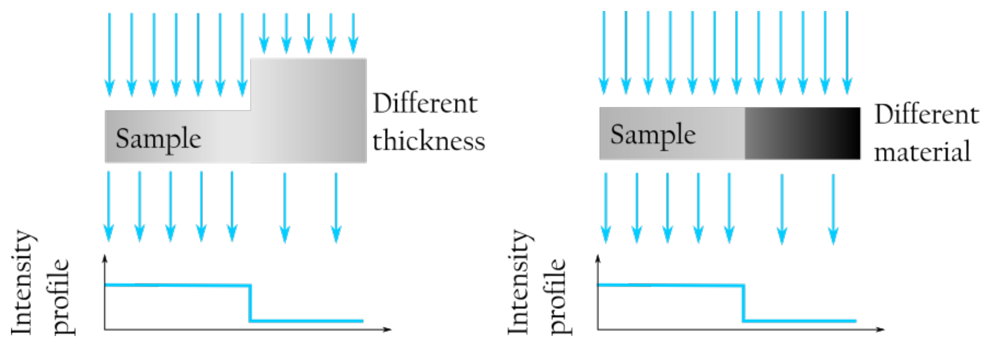

Figure 1.5: Amplitude contrast. The same intensity profile can be measured when changing either the thickness or the material of the sample.

Phase contrast

Let's now consider that no electrons get intercepted by the aperture in the back focal plane of the objective lens (which was an important assumption in the case of amplitude contrast). All the electrons thus arrive to the image plane and form the image of the specimen. Due to the scattering, however, they travelled different optical paths and thus have arrived to the image plane with a different phase. Moreover, the electrons gained a phase shift during the scattering process itself. The resulting electron wave in the image plane Ψ is given by the superposition of the individual electron waves ψ_i, $\Psi = \sum_i \psi_i$. This leads to creation of interference effects and thus intensity variations and contrast in the image.

The phase contrast is very sensitive to any small changes in either thickness, mass density, crystal orientation or even imaging properties of the system. On the other hand, when the microscope is configured and handled precisely, the phase contrast allows observation of individual atomic columns in a crystal. This delicate imaging technique is called high-resolution TEM or HRTEM. Unlike the case of amplitude contrast, the larger aperture in the objective back focal plane is used, the higher resolution of the image is obtainable.

Besides the high resolution images, the phase contrast plays an important role when imaging samples consisting of lighter elements. Since light atoms do not scatter much, the scattering angles are not high enough to produce significant amplitude contrast. Those samples (usually biological samples) are called *weak-phase objects* (WPO) and they are often approximated as objects that do not change the amplitude of the electron wave but slightly change its phase [4]. As will be discussed later, the contrast of the image of such samples is limited by the properties of the imaging system and it is often not sufficient itself. In order to enhance the contrast, phase plates are usually used. The principle of functionality and examples of such devices will be discussed in detail in section 1.4.

1.3. Imaging system of a TEM

In a transmission electron microscope, electromagnetic fields are used to control the shape and properties of an electron beam. In the particle approach which will be widely used

within this chapter, the electric field $\vec{E}$ and magnetic field $\vec{B}$ act on the electrons via Lorentz force $\vec{F} = -e\left(\vec{E} + \vec{v} \times \vec{B}\right)$, where e is the elementary charge and $\vec{v}$ is the velocity of the electron. Since fast electrons moving at relativistic speeds are used in the microscopes to achieve high resolution, the usage of electric fields to shape the electron beam sufficiently would require extremely high voltages [6]. Moreover, electrostatic lenses produce more aberrations than magnetic lenses [7]. For those reasons, magnetic lenses are used for imaging in a TEM. On the other hand, electrostatic fields are involved in the electron gun, where the highly energic electron beam is generated.

A scheme of a TEM is shown in Figure 1.6. The electrons are extracted from the electron source either by thermionic emission or by tunneling effect enhanced by an electric field acting near the source. Just below the electron source, an electrostatic lens called the gun lens is placed which controls the beam quality. Please note that this is the only electrostatic lens used in a TEM. Then, a system of electrodes accelerates the electron beam gradually to the desired kinetic energy. Most conventional transmission electron microscopes work at electron energies of 100 – 300 keV. At these energies, the electrons reach velocity of $0.55c$ for 100 keV and $0.78c$ for 300 keV. Therefore, it is necessary to consider the electrons' behavior as relativistic and to use relativistic correction to used formulas.

After passing through the acceleration system, the electron beam continues to a system of magnetic lenses. Three or four condenser lenses shape the electron beam before it hits the specimen. After the interaction, the image is magnified by a system of projection lenses and projected onto a fluorescent screen or a scintillator mounted on a CCD camera. In conventional electron microscopes, the magnification of the image can exceed 50 million [17]. In the following sections, the function of magnetic lenses and the optical design of a TEM will be discussed in more detail.

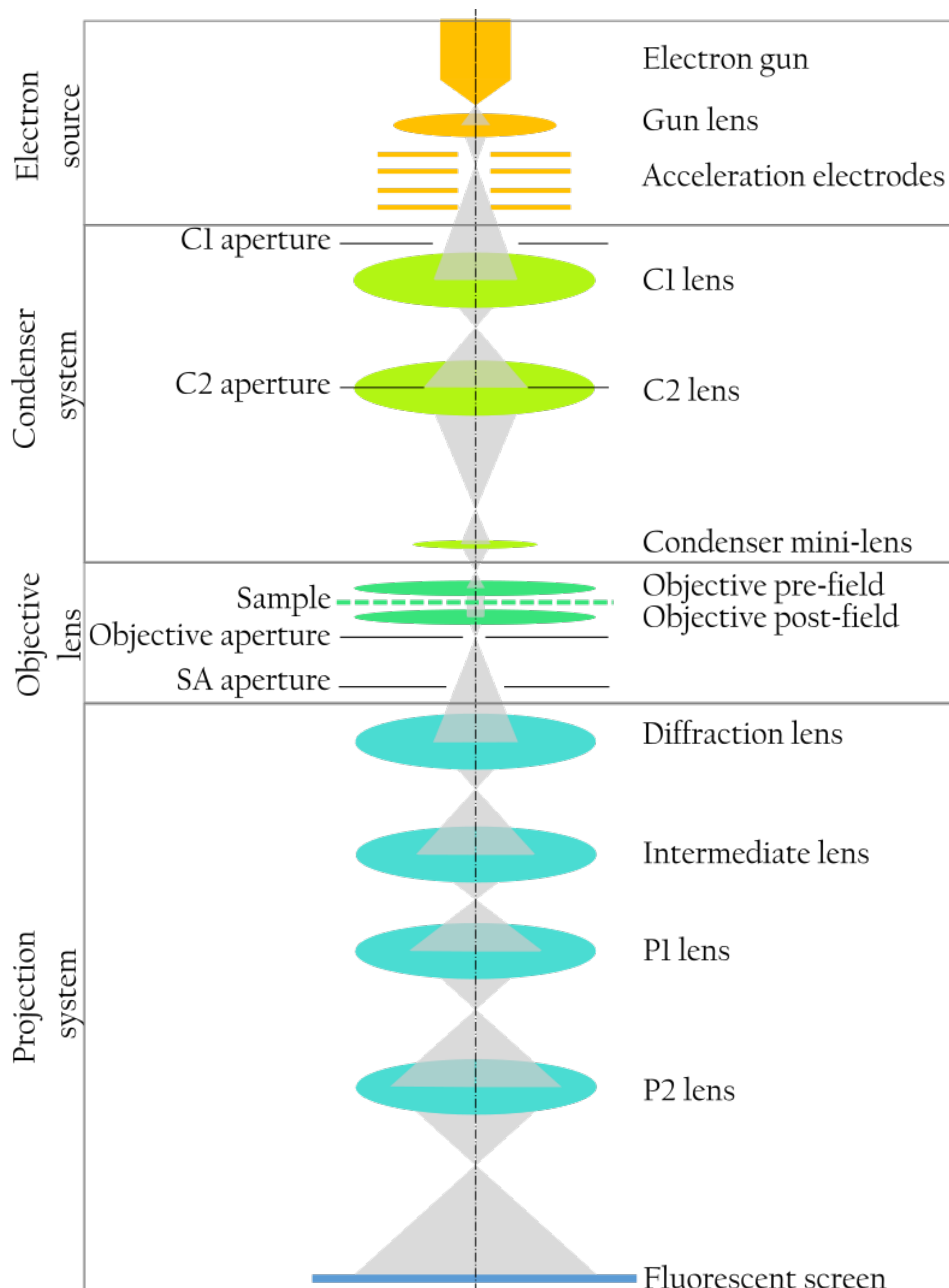

Figure 1.6: Schematic drawing of an optical system of a transmission electron microscope. On the left, the positions of the apertures and a sample are marked. On the right, the electron gun elements and magnetic lenses are marked.

1.3.1. Magnetic lenses

Magnetic lenses that are used for imaging in a conventional TEM consist of an yoke of a soft magnetic material which encloses a set of coils. The geometry of a typical magnetic lens is shown in Figure 1.7. At the inner side of the lens, the yoke [18] is terminated with two polepieces separated by a small gap. The current in the coils generates magnetic field which is channeled by the yoke into the polepieces where it escapes the magnetic material and produces intense magnetic flux around the axis of the lens. The shape of

the on-axis magnetic field is shown in Figure 1.8 and it can be described by a slightly modified Lorentz function $B(z) = B_0/\sqrt{1 + z^2/a^2}$, where the z coordinate goes along the optical axis, the field magnitude B_0 is determined by the current going through the coils and the field width a is related to the size of the gap between the two polepieces. The higher and sharper the peak of the magnetic field, the stronger the magnetic lens.

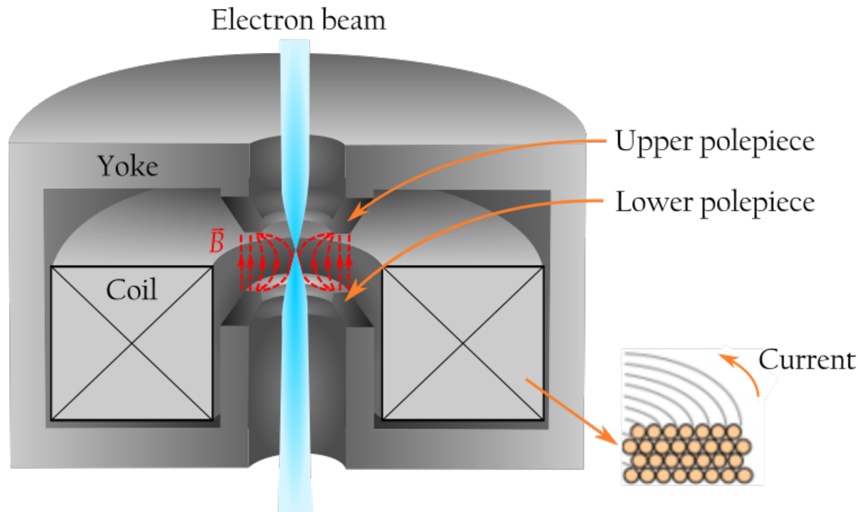

Figure 1.7: Magnetic lens. The magnetic field (red) generated by the current in the coils influences the electron beam (blue) in the area of the pole pieces. Taken and adapted from [4].

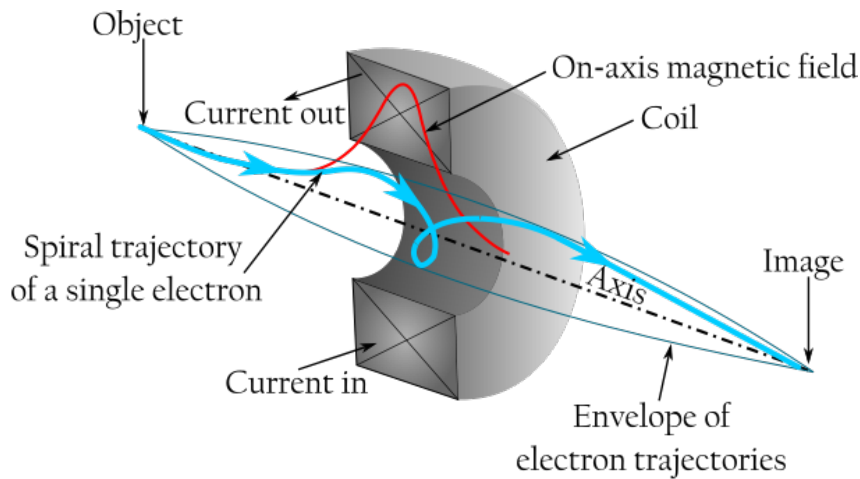

Figure 1.8: The effect of an on-axis magnetic field (red) of a lens on a single electron trajectory (blue).Taken and adapted from [5, 19].

The effect of the field of a magnetic lens on the electron trajectories is shown in 1.8. The magnetic force acts as a centripedal force resulting in a nonzero azimuthal component of the electron velocity in the magnetic field. More importantly, the inhomogeneity of the magnetic field results in a change of radial component of the velocity and thus in focusing the electron beam. In light optics, we distinguish between lenses that focus the light beam (convex lenses) and those which defocus the beam (concave lenses). However, in electron optics, only convex magnetic lenses can be designed. After leaving the magnetic field of

the magnetic lens, the electrons maintain straight trajectories. As the precise shape of the trajectories of the individual electrons is not crucial for understanding the functionality of an electron microscope, we will further consider a simplified description of the trajectories using the ray optics approach. Here, the trajectories will be represented by straight lines that only change their directions at planes corresponding to the individual lenses.

As discussed in section 1.1.2, a Fourier transform of the sample $\mathcal{F}\{\psi_S\}$ can be observed in the back focal plane, where as a perfect real-space image is formed in the image plane. Magnetic lenses, however, always suffer from aberrations which deform and blur the image. Those aberrations can be described using the so-called contrast transfer function (CTF). As the title of the function indicates, it describes how well the optical system transfers the information of spatial frequencies in the image. In other words, how the contrast at those frequencies is modified. In the BFP of the lens we thus observe the Fourier transform of the sample multiplied by the CTF. The effect of the CTF at the image plane is then given by convolution of the image and the inverse Fourier transform of the CTF $\mathcal{F}^{-1}\{CTF\}$, which is called the point spread function. The most significant aberrations of the optical system is the spherical aberration which will be discussed in more detail in the following section.

Spherical aberration

A perfect lens images a single point in the object (sample) plane into a single point in the image plane. However, the shape of the magnetic field of an electron lens causes that some rays going further from the optical axis are focused to a shorter distance than rays going close to the optical axis, as shown in 1.9. As a result, a single point is imaged as a disk of finite diameter d. The minimum cross section of the rays is called the disk of least confusion and it defines the plane of least confusion of the optical system. The position of this plane, however, is not identical with the image plane of a perfect lens (often called the Gaussian image plane).

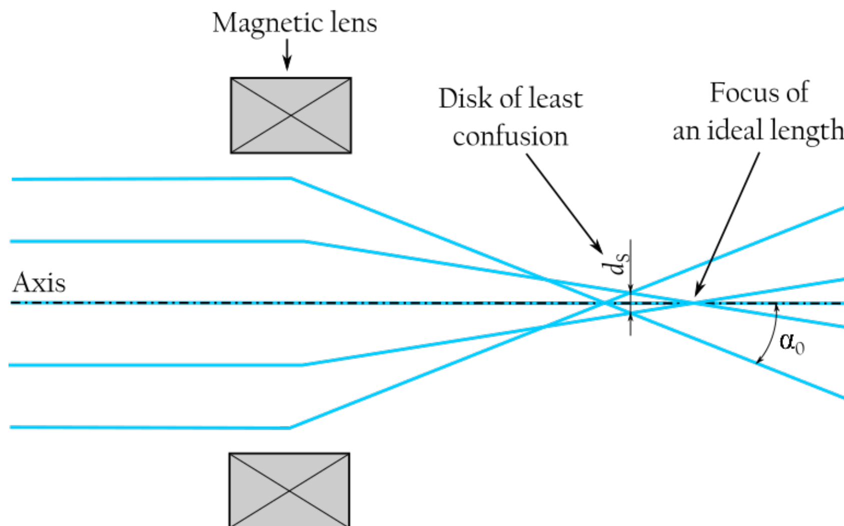

Figure 1.9: Parallel beam focused by a magnetic lens suffering from spherical aberration.

The diameter of the disk of least confusion d_{S} depends on a maximum angle of the incident rays α_0 as

$$d_{\mathrm{S}} = \frac{1}{2} C_{\mathrm{S}} \alpha_0^3.$$

Here, C_{S} is the spherical aberration coefficient and it characterizes the properties of an optical system. It is approximately equal to the focal length of a lens and for conventional magnetic lenses, it usually ranges from 0.5 mm to 2 mm. As only convex magnetic lenses (with positive focal length) can be designed, the spherical aberration coefficient is always positive. Therefore, by a combination of magnetic lenses, the spherical aberration only grows and cannot be compensated.

As the spherical aberration only influences the shape of the electron wave and not the overall intensity, it can be also described as an additional phase shift of the electron wave. The phase shift $\Delta\phi_{\mathrm{S}}$ depends on the scattering angle θ as [20]

$$\Delta\phi_{\mathrm{S}}(\theta) = \frac{\pi}{2\lambda} C_{\mathrm{S}} \theta^4.$$

The ratio of an electron wave projected by a system suffering from spherical aberration ψ_{S} and an electron wave projected by a perfect optical system ψ is thus given by

$$\frac{\psi_S}{\psi} = \mathrm{e}^{\mathrm{i}\Delta\phi_{\mathrm{S}}(\theta)} = \mathrm{e}^{\mathrm{i}\pi C_{\mathrm{S}} \theta^4 / 2\lambda}.$$

In modern electron microscopes, the spherical aberration significantly limits the achievable resolution. Because of its strong dependence on the angle of the incident beam, apertures in the order of 10^2 μm are used in the microscope in order to eliminate high-angle electrons. It has been proven that the coefficient of the spherical aberration of a radially symmetric magnetic lens is always positive [4]. As a result, the aberrations of multiple lenses of this type only accumulate and can never be compensated by a suitable combination of optical elements [21]. When breaking the rotational symmetry by introducing multipole magnetic devices, the spherical aberration can, however, be partially compensated. Hence, in modern microscopes, hexapole and octupole pieces are used as spherical aberration correctors. The microscopes using such correctors are labeled as aberration-corrected microscopes and they can reach sub-Ångstrom resolution [22, 23].

1.3.2. TEM optical system

The optical system of a conventional TEM consists of 8 – 9 magnetic lenses, which can be divided into 2–3 sections regarding their position with respect to the sample. A schematic picture of the optical system is shown in Figure 1.6. The first three lenses make up the condenser system of the microscope which forms the electron beam before it hits the sample. The sample is placed between the polepieces of the objective lens which creates the first image of the sample. The remaining lenses form the third section of the TEM optics, the projection system. They further magnify the first image of the sample and project the final image onto a fluorescent screen. Here, the image can either be observed directly by the user or recorded by a camera.

The first condenser lens (C1) creates an image of the virtual crossover of the electron source and its excitation determines the size of the electron probe on the sample. The second condenser lens (C2) is then used to change the size of the illumination area. When the narrow electron probe is achieved, we state that the C2 lens is focused; by defocusing the lens, parallel illumination can be achieved. In modern microscopes, a third condenser lens, called the condenser mini-lens, is usually involved. It works in a dual mode, switching between two imaging modes - **nanoprobe** (switched off) and **microprobe** (switched on). The condenser mini-lens is physically placed in the upper polepiece of the objective lens and thus the effective field of the lens is given by the combination of the magnetic field of the mini-lens and of the objective. The mode-switching is then achieved by changing the polarity of the current in the mini-lens. When the current has the same polarity as the objective lens, the mini-lens is optically switched on. When the polarity is opposite, the mini-lens is optically switched off.

The microprobe is usually used in the standard TEM mode where the sample is illuminated by a parallel electron beam and the whole illuminated area is observed at the same time (see in Figure 1.10 on the left). Here, the presence of the third condenser mini-lens enables illumination of a broader area. On the other hand, the nanoprobe is used for scanning TEM (STEM) applications as it provides a more focused electron probe, which is then scanned over the sample (see in Figure 1.10 on the right).

In the condenser system, two apertures are inserted. The first one is placed above the C1 lens and is thus called the C1 aperture. It is used to reduce the angle of divergence of the electron beam to limit the effect of the spherical aberration. The next aperture is placed right in the middle of the C2 lens and it is called the C2 aperture. It determines the size of the illuminated area of the sample when the parallel illumination is used.

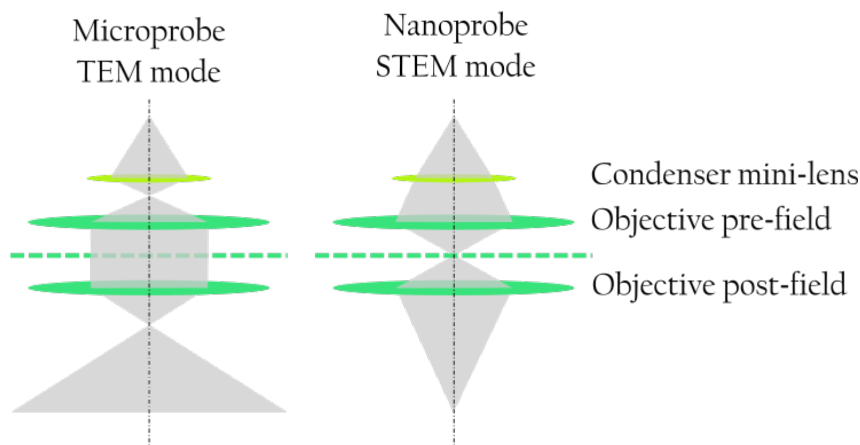

Figure 1.10: Comparison of the microprobe and nanoprobe applications. The left part of the image shows the microprobe mode, where the condenser mini-lens is optically switched on and it is generally used in TEM applications. On the right side, the nanoprobe mode is shown, where the condenser mini-lens is optically switched off and it is generally used in STEM applications.

The objective lens is the strongest lens in the microscope and it can be considered to be the most important one. Although it creates only one peak of the magnetic field between the two polepieces, it acts optically as two lenses. The upper virtual objective

lens is usually called the objective pre-field or condenser-objective lens; the lower lens is then called the objective post-field or simply the objective lens [4, 6, 24]. The sample is placed between the two polepieces. As the image produced by the objective lens is further magnified by the projection system, the effect of the objective aberrations is magnified too. Therefore, it is fair to state that the objective lens determines the quality of the final image [4].

As the focal length of the objective lens is very short (in the order of millimeters), the back focal plane is physically situated between the two polepieces. Thus, in the physical design of the objective lens, two holder entries are present – one for a sample holder, and the other either for a objective-aperture holder or for phase plate holder (which will be discussed later). In standard TEM imaging settings, the objective aperture is retracted. However, in some applications it can be inserted in order to enhance the amplitude contrast, as discussed in 1.2.2.

The first lens of the projection system is called the diffraction lens and it determines what type of image is observed at the fluorescent screen. In the so-called imaging mode, the intermediate lens is focused into the first image plane, projecting the real-space image of the sample. In the diffraction mode, the lens is focused into the back focal plane of the objective lens where the Fourier image of the sample is formed. In the first image plane, an aperture can be placed in order to reduce the area of the sample that would be further imaged. This aperture is called selective area aperture, or SA aperture shortly.

The remaining two or three projection lenses (called intermediate, P1 and P2 lens) then further magnify the image created by the intermediate lens and project it onto the fluorescent screen. In conventional TEMs, a predefined set of magnifications is available. There, the excitations of the individual projection lenses are set in such a way that the image remains focused and rotation-free when switching between the magnifications.

In standard TEM applications, the image of the whole illuminated area of the sample is produced at the same time and recorded by a CCD camera. In the STEM applications, where a single spot of the sample is imaged at the time, more complex set of detectors are used. The on-axis circular detector collects the primary-beam electrons and produces a so-called bright-field image. An angular detector surrounding the bright-field detector then collects the low-angle scattered electrons, generally originated from diffraction, and produces a dark-field image. The electrons scattered at higher angles are then collected by the so-called high-angle annular dark-field detector.

1.4. Phase plates

Specimens consisting of lighter atoms, such as biological samples, can be described in the terms of the weak phase objects approximation. Hence, the electron wave does not experience a change of amplitude induced by the interaction with the sample and it only obtains a small phase shift with respect to the primary wave [4]. The contribution of the amplitude contrast in the image is thus neglected and only the phase contrast is considered. However, due to only small phase shift induced by the sample, the resulting contrast in the image is considerably small.

In order to improve the phase contrast, the phase shift between the unscattered and scattered electrons needs to be enhanced. The devices used for this purpose are called phase plates (PPs), and can work on various principles. The PP is placed in the back focal plane of the objective lens, where scattered and unscattered electrons can be easily distinguished. In this plane, the distance r of an electron from the optical axis is related to the spatial frequency q of which the electron carries the information as $r = qf\lambda$, where f is the objective's focal length and λ is the electrons' wavelength.

In the following, the theoretical background of the PP contrast enhancement will be presented. Afterwards, an overview of different PPs developed recently will be shown and the advantages and disadvantages of particular designs will be discussed.

1.4.1. Contrast transfer function

As was mentioned previously, electrons scattered from the sample carry information about different spatial frequencies q. This information is then transferred by a projection system into the image. However, the aberrations of the projection system limit the quality of the information transfer. In a rotationally symmetric system, spherical aberration and defocusing have the most significant effect on the transferred contrast. The contrast transfer function of the system is then given by [25]

$$F(q) = A(q)[\sin\gamma(q) - W\cos\gamma(q)], \tag{1.19}$$

where $A(q)$ is the envelope function including the effect of partial coherence of the electron beam in a real setup and causes attenuation of the contrast at higher spatial frequencies, W is the ratio between the amplitude contrast and the phase contrast and $\gamma(q)$ describes the effect of the aberrations as

$$\gamma(q) = 2\pi\left(\frac{1}{4}C_{\mathrm{s}}\lambda^3q^4 - \frac{1}{2}\Delta z\lambda q^2\right). \tag{1.20}$$

Here, C_{s} is the coefficient of the spherical aberration, Δz is the defocus, and λ is the electron wavelength.

As the amplitude contrast is negligible in the case of biological samples, we can further consider $W \approx 0$. The function $\sin\gamma(q)$ thus determines the shape of the resulting contrast transfer function. In Figure 1.11 (a), this function is plotted for an 80 keV electron beam, $C_{\mathrm{s}} = 1.3$ mm and various Δz [26]. We can see that by varying the defocus, the range of spatial frequencies being transformed with high contrast can be optimized [27]. However, the transferred contrast remains very low at low frequencies, which means that larger objects are harder to distinguish in the image.

An ideal PP performs a phase shift of $\varphi = \pm\pi/2$ of all the scattered electrons ($q \neq 0$), keeping the phase of the unscattered electrons. Hence, we get a new relation for the contrast transfer function

$$F(q) = A(q)\sin[\gamma(q) \pm \pi/2] = \pm A(q)\cos\gamma(q). \tag{1.21}$$

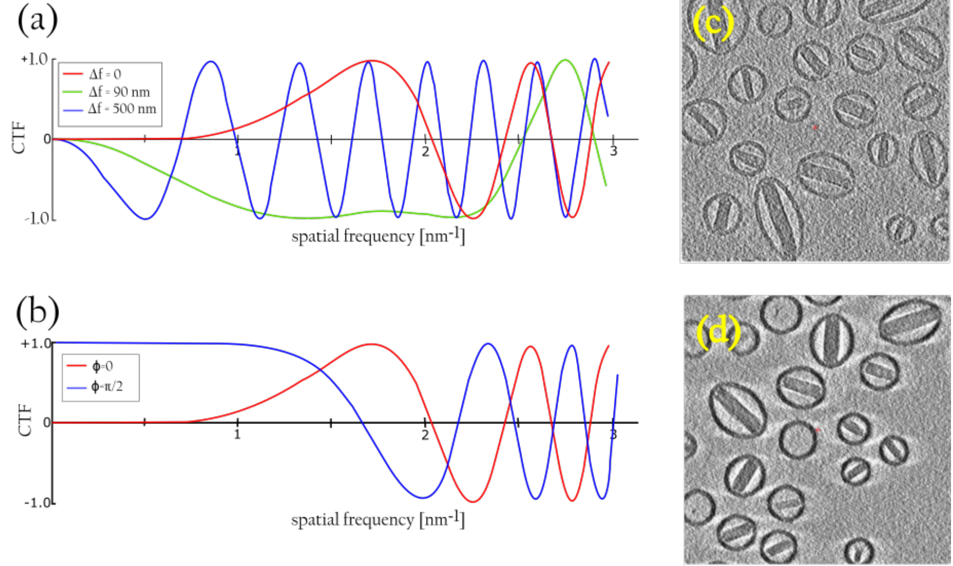

Figure 1.11: (a) Function $\sin(q)$ for differing values of defocus. (b) The effect of the phase plate on the contrast transfer function. (c) and (d) TEM images taken with and without a phase plate, respectively [28].

The effect of the phase shift of $-\pi/2$ on both the CTF and the image is shown in Figure 1.11 (b). As the contrast gets higher at lower spatial frequencies, it is easier to distinguish larger structures in the image, such as individual cells.

1.4.2. Thin film phase plates

The most straightforward concept of a PP is based on a thin layer of material placed in the back focal plane. Here, the phase shift is induced by the interaction of the electrons with the electrostatic potential fields $V(x,y,z)$ of the atoms in the material. The phase of an electron beam gained when passing through the material along the z axis can be calculated using the WKB approximation introduced in section 1.1.1. Assuming a material homogeneous in x and y, the phase is given by

$$\phi(x,y) = \pm \int_{\text{sample}} \frac{\sqrt{2m(\mathcal{E} - V(x,y,z))}}{\hbar} \mathrm{d}z,$$

where m is the relativistic mass of an electron, $\mathcal{E}$ is the relativistically corrected total electron energy. As the energy of the primary beam in a TEM is in the hundreds of keV and the inner potential of a material is usually in tens of eV [29, 30], the argument of the integral can be simplified using formula $\sqrt{1+x^2} \approx 1 + \frac{x^2}{2}$. Hence, the phase can be written as

$$\phi(x,y) = \pm \frac{\sqrt{2m\mathcal{E}}}{\hbar} \int_{\text{sample}} \left(1 - \frac{V(x,y,z)}{2\mathcal{E}}\right) \mathrm{d}z.$$

For a homogeneous sample with a thickness much larger than the interatomic distances, the integral can be replaced by a product of the sample thickness t, elemental charge e and so called mean inner potential U_{mean}. Substituting the relations for the relativistically

corrected energy and mass of an electron, the phase difference of an electron beam passing through vacuum and a beam passing through the sample is given by

$$\Delta\phi(t) = \frac{\pi e}{\lambda}\frac{U_{\text{mean}}}{E}\frac{E_0 + E}{2E_0 + E}t, \tag{1.22}$$

where λ is the wavelength, E_0 the rest energy and E the kinetic energy of an electron [31]. For a chosen material and given electron beam properties, the desired phase shift is thus achieved by optimizing the thickness of the PP.

To avoid additional scattering and coherent diffraction effects, the layer should consist of a light material and should be amorphous. Moreover, the material needs to be conductive to avoid charging. In most applications, amorphous carbon is used as a PP. However, some experiments with metal-covered silicon layer [32] have been performed to reduce the charging effect. In aim to limit the contamination growth degrading the functionality of the PP, the material needs to be heated up to prolong the PP lifetime.

The first introduced concept of a thin film PP is inspired by the PP used in light-optics microscopes [33]. The so-called *Zernike PP* consists of a homogeneous layer of a material with a circular pinhole aligned with the TEM's optical axis. The scattered electrons traverse the layer of material and experience a phase shift of $\pi/2$ with respect to the unscattered beam [34]. The most obvious disadvantage of this design is the need of a very precise alignment of the pinhole with the optical axis of the TEM. Moreover, the sharp jump in phase together with charging of the material around the pinhole edge results in an unwanted halo [35].

Another PP design, the *Hilbert's PP*, consists of a hemicircular plate providing a phase shift of π instead of $\pi/2$ [36, 37, 38]. A reduction of the 2D problem into 1D simplifies the alignment procedure of the PP significantly. However, it also results in reducing the contrast enhancement into one direction. Thus, we can see a shadow in the direction perpendicular to the edge of the PP creating topographic image of the sample.

In present days, the most popular thin film PP is the *Volta PP* discovered independently by Malac [39] and Danev [40]. The PP consists of a homogeneous layer of material and the phase shift is created by a local primary beam-induced change of the material properties. Depending on the sample properties such as material or temperature, the primary beam induces either negative or positive charge at the PP's surface. The induced screening potential has a different spatial distribution leading to an electrostatic field acting on the primary beam and creating a phase shift with respect to the scattered electrons. The main advantage of this PP is the self-alignment with the primary beam. On the other hand, the phase shift is time dependent. Thus, it is needed to let the PP stabilize for some time before image acquisition, and to only use the PP for few hours at a time.

1.4.3. Electrostatic phase plates

Another PP concept, originally introduced by Hans Boersch in 1947 [41], takes the advantage of the effect of an electrostatic field on electrons. The phase shift of the electrons induced by a potential spatial distribution $V(x, y, z)$ is given by

$$\phi(x, y) = \pi \frac{1}{\lambda E} \frac{E_0 + E}{2E_0 + E} \int V(x, y, z)\mathrm{d}z. \tag{1.23}$$

This effect can be then used within a PP if a localized potential is created in the focal point of the objective lens.

Initially, Unwin used a small aperture with a thin poorly conducting thread spanning its diameter to generate the electric field [42]. Due to high currents around the focal point, the thread charges locally by the incident electron beam resulting in local negative potential acting on the unscattered electrons. The main advantage of this PP is that the alignment is only crucial in one direction [43]. On the other hand, the thread needs to be thinner than the diameter of the focused primary beam so that part of the electrons can pass around, which results in high manufacturing demands. Furthermore, the image suffers from the diffraction of the primary beam on the thread.

Most of the modern electrostatic PPs are based on an unipotential lens consisting of three electrodes, where the two outer ones are set to zero potential with respect to the vacuum level and the inner one is at a higher potential V. As a result, the electrons passing through the lens experience a phase advance while maintaining their kinetic energy. The phase shift is determined by the potential on the inner electrode and thus it is fully adjustable.

The most common design of such a PP is so called *Boersch PP*. It consists of a small cylindrical unipotential lens being attached to its surroundings by few supporting arms [44, 45, 46], see Figure 1.12(b). The unipotential lens is realized via a five-layers structure, where the outer-most layers and the central layer are made of metallic electrodes connected to defined potentials, and the intermediate layers create an insulator shielding. As both the scattered and unscattered electrons pass through vacuum, no additional scattering is obtained. However, the ring of the unipotential lens obstructs a significant part of the frequency spectrum at low frequencies.

To overcome this problem, a new concept of a PP was suggested by Zach [47]. The design of the so-called *Zach PP* is analogous to a microcoaxial cable [48, 49]. A metallic electrode is led through an insulating layer surrounded by metallic covering (see Figure 1.12(c)). The inner electrode is set to a higher potential with respect to the covering and thus local electric field is generated around an open end of the cable. As the ending of the cable is then placed to the vicinity of the focal point of the objective lens, the unscattered electrons experience a local electric field and obtain a phase shift. The main advantage of this design is that the PP's supports obstruct only a small part of the scattered electrons. On the other hand, the electric field is not homogeneous anymore and the supportive structure of the cable still obstructs electrons scattered in the direction of the cable. As a result, directional contrast is created in the image.

Another design of an electrostatic PP, so-called *anamorphic PP*, offers a completely obstruction-free solution [50, 51]. The electron beam in a diffraction plane is shaped in a

thin stripe and passes through a rectangular slit. In the middle of the slit, an unipotential lens is placed as drawn in Figure 1.12(d). As a result of the geometrical setup, only unscattered electrons and electrons scattered along the direction perpendicular to the slit orientation are phase-shifted. The procedure is then repeated in another diffraction plane of the imaging system in the perpendicular direction. The inner electrodes of both lenses are set to such a potential that the electron beam passing through obtain the phase shift of $\pi/4$. Thus, the resulting phase shift between the unscattered beam and the electrons scattered in an arbitrary direction reaches $\pi/2$. An exception takes place for the electrons scattered in one of the two orientations of the rectangular slit, where the phase shift only reaches $\pi/4$. The main advantage of this design is the absence of any obstructing or scattering hardware. However, new imaging system needs to be developed and integrated into a TEM in aim to shape the beam into the stripes.

1.4.4. Magnetic phase plates

Magnetic PPs take advantage of the Aharonov-Bohm effect, which was described in section 1.1.1. The effect of a magnetic field $\vec{B} = \vec{\nabla} \times \vec{A}$ on electron phase is similar to the effect of an electric field. Assuming a vector potential of the field $\vec{A} = (A_x, A_y, A_z)$ and an electron travelling along the z direction, its phase will be changed by

$$\phi(x, y) = \frac{e}{\hbar} \int A_z(x, y, z) \mathrm{d}z,$$

where e is the elemental charge and $\hbar$ is the reduced Planck's constant [52]. The magnetic PPs' design thus aims to generate a strong longitudinal vector potential field at the optical axis and to minimize the strength of the field beyond the axis.

A magnetic ring carrying a magnetic field circulating in the azimuthal direction provides a vector potential field circulating perpendicular around the ring [53, 54, 55], see Figure 1.12(e). At the optical axis, the field strength is maximal, and it points parallel with the optical axis, which results in a strong phase shift of the unscattered electrons. However, due to a very short focal length of the objective lens, the objective's strong magnetic field penetrates significantly into the back focal plane and thus influences the field of the magnetic ring. Therefore, the ring needs to be made of a material with high coercivity or placed in a conjugated diffraction plane further from the objective lens. Similar to the Boersch electrostatic PP, the magnetic ring and the supportive construction represent an obstructing hardware. However, the radial width of this ring is much smaller (tens of nanometers).

The *tunable Ampere PP* uses a current-carrying wire going parallel to the incident beam along the optical axis. The wire generates a current-dependent phase-shifting field given by Ampere's law on electrons passing close to the wire. In the work of [56], the PP was realized by a wire in the form of three orthogonal segments, where the middle segment goes parallel to the optical axis and generates the phase shift of the electrons, and the two outer segments connect the middle segment to the PP support, see Figures 1.12(f) and 1.12(g). As the wire represents obstructing hardware, the middle element cannot be perfectly aligned with the optical axis and needs a slight offset. The main advantage of this design is the tunability of the phase shift by the change of the electric current passing

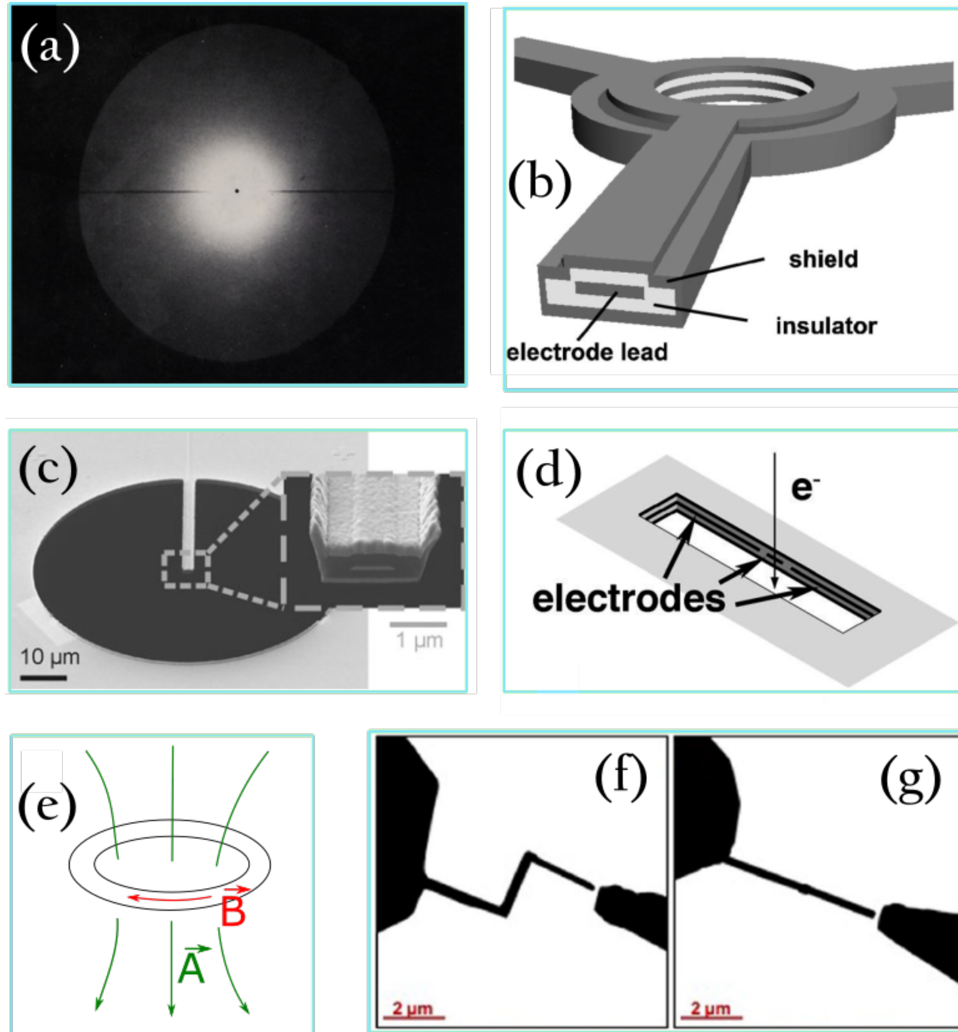

Figure 1.12: (a) TEM image of the Unwin PP placed at the back focal plane of the objective lens. The black dot in the center is drawn to indicate the typical size of the beam of unscattered electrons (Magn. 3000x). [43]. (b) Three-dimensional sketch of the Boersch PP's central region [44]. (c) Scanning electron microscope image of a Zach PP [49]. (d) Geometry of the anamorphic PP [50]. (e) Schematic drawing of the spatial distribution of magnetic field and vector potential of a magnetic ring PP. (f) and (g) Bright-field images of the tunable Ampere PP viewed in the specimen plane in a TEM at tilt angles of 70° and 0° with respect to the optic axis of the microscope, respectively [56].

through the wire. However, the lack of symmetry of this design results in inhomogeneous phase contrast enhancement.

1.4.5. Phase plates comparison

To this date, many theoretical and experimental works have been presented in PP development. The results included in those works show a great contrast enhancement in the images of biological samples, making it easier to distinguish the structures in the

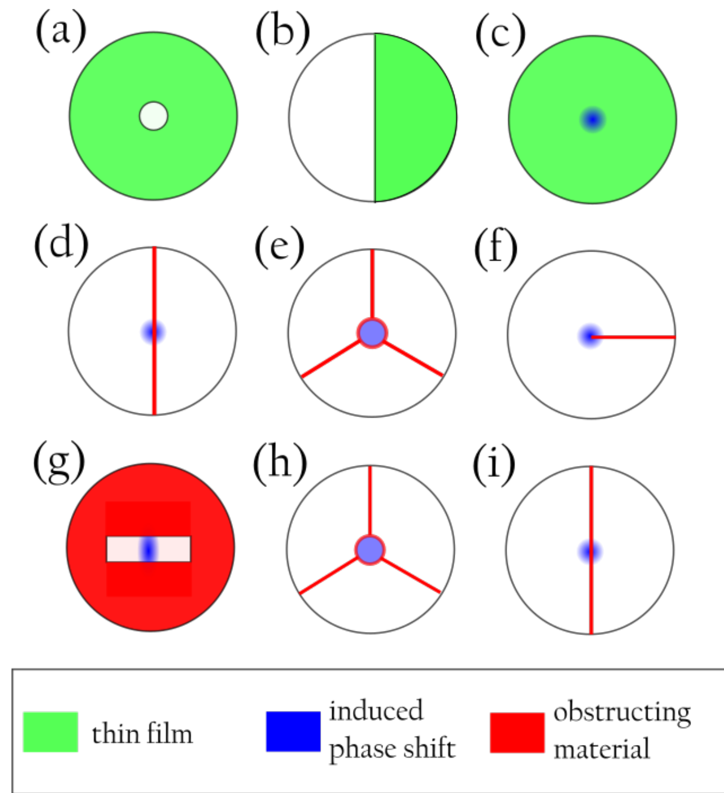

Figure 1.13: (Schematic drawings of individual phase plates mentioned in the article. (a) Zernike PP (b) Hilber PP (c) Volta PP (d) Unwin PP (e) Boersch PP (f) Zach PP (g) anamorphic PP (h) magnetic ring PP (i) tunable Ampere PP.

images. However, all the presented concepts face difficulties related to their realization design. Thin film PPs produce additional electron beam scattering and do not provide a tunable phase shift. Moreover, they suffer from contamination which reduces their lifetime significantly. Unipotential lens-based PPs offer the convenience of a tunable phase shift but require a complex fabrication procedure. Furthermore, most electrostatic PPs need obstructing hardware that limits information transfer for specific spatial frequencies. Problems with obstructions are also related to the magnetic PPs. The anamorphic PP might solve this problem as it avoids any obstruction and scattering. However, it requires an entirely new optical design and thus cannot be implemented to conventional TEMs.

Zernike PP

Hilbert PP

Volta PP

Unwin PP

Boersch PP

Zach PP

anamorphic PP

magnetic ring PP

tunable Ampere PP

Disadvantages

1D alignment

2D alignment

Scattering

Obstructing

TEM modification

Advantages

Tunable phase shift

Figure 1.14: Overview of the advantages (tunability) and disadvantages (alignment, scattering, obstruction, TEM modification) of the individual phase plates presented.

Chapter 2

Phase plate implementation

In commercial electron microscopes, thin film-based phase plates are used. In microscopes provided by Thermo Fisher Scientific Inc., the Volta phase plate is implemented [57], while in microscopes made by JEOL Ltd., the Zernike phase plate is used [58]. These phase plates are made of an amorphous carbon layer which has to be heated to the temperature of approximately 200 °C to avoid contamination growth. As discussed in section 1.4, no wider research of materials that could be used instead of carbon has been done so far. Thus, the main goal of this thesis is to design an experiment to measure the effect of different materials and different conditions on the phase of an electron wave. The experiments are designed for microscope series Talos provided by Thermo Fisher Scientific.

2.1. Phase shift measurement designs

A phase of a wave is a relative value and it cannot be measured directly. Therefore, a comparative measurement technique needs to be applied. In the following sections, three such techniques will be introduced – an electron biprism-based holography measurement, a measurement using a diffraction grid and a defocused-image analysis. All these techniques take an advantage of splitting the electron beam into two paths and then overlapping them in the image plane.

2.1.1. Electron biprism

In 1948, a Hungarian-British physicist Dennis Gabor introduced a new imaging technique that would enable to capture both the amplitude and the phase of electrons, which is nowadays generally known as electron holography [5, 59, 60]. This technique is based on the interference of an electron wave carrying the sample information with a reference wave. In light-optics experiments, a glass biprism is used to divide a coherent light beam into two halves and overlap them to create the interference pattern. As the two halves of the beam go off the optical axis, this technique is called off-axis holography. In electron microscopy, the electrostatic biprism is used to achieve the same effect. It consists of a very thin charged filament placed between two grounded electrodes.

The conventional setup used in electron holography is shown in Figure 2.1. The specimen is placed in such a way that only half of the parallel electron beam passes through it. The beam is then focused by the objective lens. The electrostatic biprism is placed below the beam crossover with the filament crossing the optical axis perpendicular to the beam. The voltage applied to the filament is usually in the range of 15-25 V [61, 62]. As the filament goes parallel to the edge of the specimen, it divides the beam effectively into two halves, where one of them carries the information about the sample (sample wave) and the other one corresponds to the original electron wave (reference wave). The filament is connected to high voltage with respect to two grounded electrodes positioned in the same plane along the optical axis, so that the resulting electrostatic field bends the electrons trajectories towards the optical axis. As a result, the sample wave and the reference wave overlap and create an interference pattern.

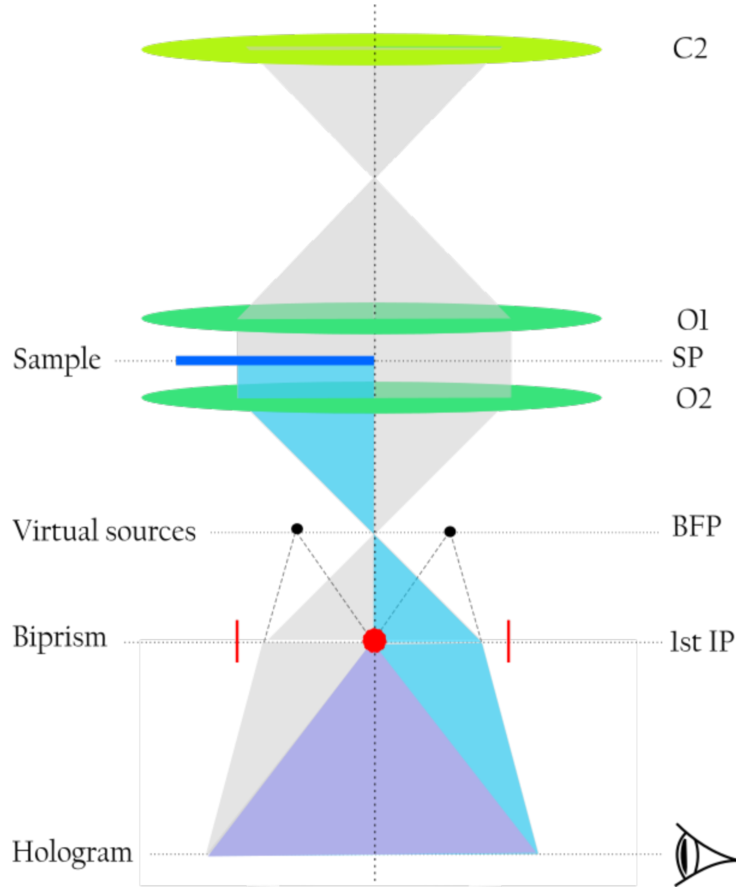

Figure 2.1: Electron holography. The electron beam passes through the TEM optical setup (marks on the right). The sample (dark blue) covers half of the sample plane (SP). Consequently, the electron wave is split into the reference wave (grey) and the sample wave (light blue) below the sample plane. Those two waves are then bent by the electron biprism (red). As a result, a pair of virtual sources (black dots) is produced in the back focal plane (BFP) and the two waves overlap and produce a holograph (purple) which is then detected (eye mark).

To describe the intensity distribution of the pattern, we will suppose the reference wave to be a plane wave $\psi_r = \psi_0 e^{i\vec{k}_r \cdot \vec{r}}$, where ψ_0 is the wave amplitude, $\vec{k}_r$ is the wave

vector and $\vec{r}$ is the position vector. As the sample wave ψ_s interacts with the specimen, the amplitude is modulated by a factor a_s and the phase gets shifted by ϕ_s. Thus we get $\psi_s = a_s \psi_0 e^{\mathrm{i}(\vec{k}_s \cdot \vec{r} + \phi_s)}$, where the sample wave vector $|\vec{k}_s| = |\vec{k}_r|$ is symmetric to the reference plane wave vector across the optical axis. The intensity in the observation plane perpendicular to the optical axis is then given by the superposition of the reference and the sample wave as

$$I = \left| \psi_0 e^{\mathrm{i}\vec{k}_r \cdot \vec{r}} + a_s \psi_0 e^{\mathrm{i}(\vec{k}_s \cdot \vec{r} + \phi_s)} \right|^2 = |\psi_0|^2 \left\{ 1 + a_s^2 + 2a_s \cos\left[2\pi \frac{x}{d} + \phi_s \right] \right\} \tag{2.1}$$

where x goes parallel to $\mathbf{k_r} - \mathbf{k_s}$ and the fringe spacing d is proportional to the wavelength of the electrons and to the reciprocal value of the electron biprism voltage.

The intensity of the interference fringes is thus given by the amplitude modulation of the sample wave, while the phase shift determines the spatial position of the fringes. This results in an image containing areas of mutually shifted fringes of different intensities which correspond to different sample areas. In order to measure the phase shift induced by an examined material, two measurements need to be performed – one with a sample inserted and one without. The spatial shift of the interference patterns is then to be analysed.

The electron biprism is a key component of the electron holography technique. To guarantee proper functionality of the device, the charged wire needs to be homogeneous, very thin and have a high conductivity. The fabrication of the wire is thus a rather complicated task and the result is very sensitive to the fabrication accuracy. Possible fabrication methods involve photolithography [62], focused ion beam lithography [63], quartz rod drawing over a flame [64], or by using a spider thread [65]. As those procedures are complex and beyond the scope of this thesis, a commercial electron biprism would be used in the experiment. However, due to difficulties with the biprism supplier, the component was not available within this project. Therefore, different, unconventional phase-shift measurements were performed.

2.1.2. Diffraction grid beam splitting

The electron biprism used in conventional holography measurements can be replaced with a diffraction grid. An electron beam diffracted by a grid produces a set of diffraction orders labeled by an integer n and propagating under angles θ_n determined by $n\lambda/\Lambda = \sin\theta_n$. Here, λ is the electron wavelength and Λ is the spatial period of the diffraction grid. A sample is placed in such a way that only a part of the diffraction orders pass through it (object wave) and the remaining orders pass through vacuum (reference wave). A magnetic lens placed below the sample, focusing the diffracted beams and producing an area where the beams overlap and create an interference pattern introduced in (2.1). The fringe spacing d is determined by the electron wavelength and the spatial frequency of the diffraction grid. Just like in the case of the measurement with an electron biprism, two measurements need to be performed and compared to determine the spatial shift of the interference fringes due to the presence of a sample and thus the phase shift of the electron wave induced by the sample.

The experiments using a diffraction grid are described in detail in [66, 67]. There, the grid is placed in the plane of a condenser aperture and illuminated by a parallel electron beam. The diffracted beams are then focused by a lens and in the back focal plane, they create separate maxima corresponding to the diffraction angles. The profile of the diffraction grid is optimized to produce strong first order maxima and negligible maxima of higher orders. The following lens then creates an image of the diffraction grid where the reference wave overlaps with the phase-shifted object wave.

In TEMs of the Talos series, a sample and a diffraction grid can be placed in one of the holders already implemented in the microscope. Besides the standard sample holder, aperture holders can be used as well, namely C1, C2, objective and SA apertures holders (see Figure 1.6). In the experiment designs introduced below, only the C2, sample and objective holders are taken into account.

In the Figure 2.2, the cutout of the Talos optical system with approximate geometrical parameters is shown. As the exact parameters of the microscope are confidential, the positions of the lenses are only rough estimates based on the outer construction of the microscope. The focal length of the objective lens in TEMs is usually in the range of 1 mm to 5 mm [68, 69, 70]. The magnification provided by the objective lens is then in the range of 20 to 50 [24]. In the following considerations, the focal length of the objective lens is estimated to be $f_\mathrm{O} = 2.5$ mm and the magnification to $M_\mathrm{O} = 40$.

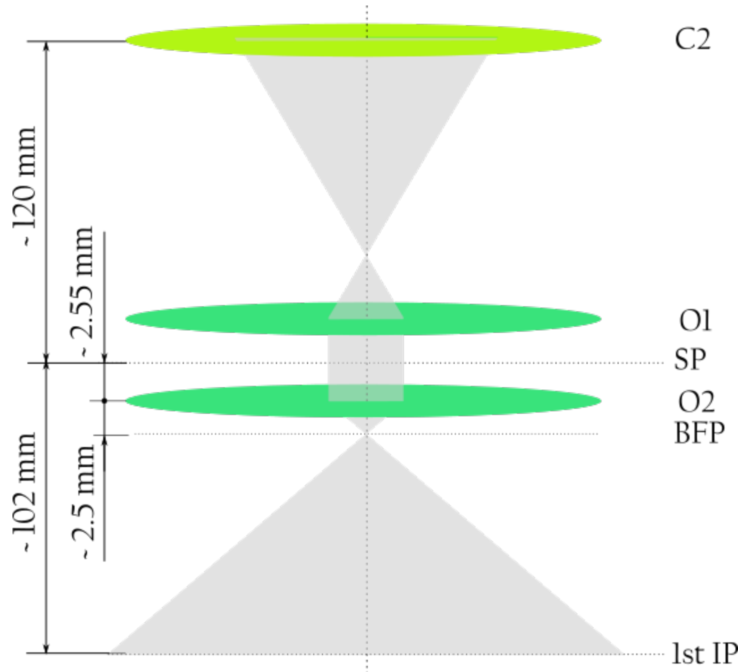

Figure 2.2: The cut-off of a microscope of Talos series with optical elements relevant for the experimental designs and with approximate geometrical parameters.

In the first design (see Figure 2.3), the diffraction grid is placed in the sample plane and is illuminated by a parallel electron beam (TEM mode). In the BFP of the objective lens, diffraction maxima are produced. The sample is placed in the BFP, occupying a half plane off the optical axis. The interference pattern is then produced in the image plane of

the objective lens. As the electron beam is focused on the sample, this design is suitable for the Volta PP experiments.

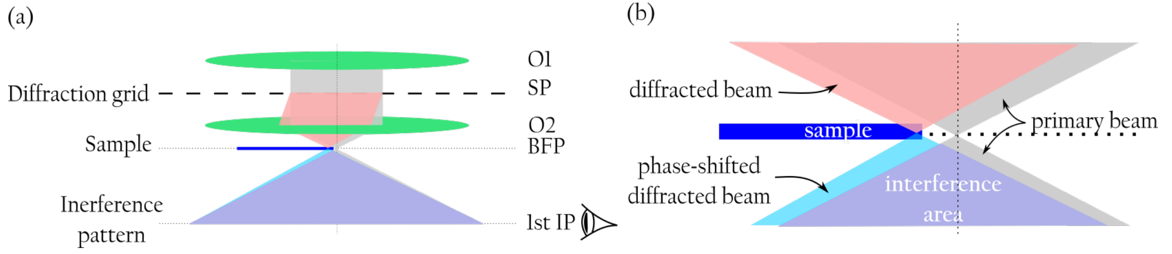

Figure 2.3: (a) First measurement setup with a diffraction grid in the sample plane and a sample in the back focal plane. The diffraction grid generates diffraction maxima represented by one first-order maximum (red). The maximum passes through the sample (dark blue) and obtains a phase shift. The phase-shifted beam (light blue) interferes with the primary beam (grey) and produces an interference pattern (purple), which is detected (eye mark) in the first image plane. (b) A detailed view of the beams around the sample.

For small diffraction angles ($\sin\theta \approx \theta$), the spacing D of the diffraction maxima in the BFP is determined by the periodicity of the grid Λ and by the focal length of the objective lens f as

$$D \approx f\frac{\lambda}{\Lambda}.$$

The diffraction grid can be created using a focused ion beam (FIB) milling, where the highest achiavable resolution is around 5 nm [71]. The smallest grid periodicity is thus in the order of 10^1 nm. Considering the focal length of the objective lens is around 1-2 mm and the electron wavelength at 200 keV is 2.5079 pm, the largest achievable spacing of the diffraction maxima in the BFP is approximately 625 nm. This would require a very precise alignment of the sample in the BFP with respect to the position of the maxima, which is barely achievable by the aperture alignment mechanism in the microscope. In order to overcome this difficulty, the diffraction grid can be replaced with a monocrystalline material. The typical interatomic distances in monocrystals are in the orders of angstroems, i.e. two orders of magnitude smaller than the achievable FIB-milled diffraction grid. Therefore, the spacing of the diffraction maxima can reach up to 50 µm. However, in order to guarantee the creation of strong diffraction maxima, correct orientation of the crystal with respect to the optical axis has to be provided.

In the other design (see 2.4), the diffraction grid is placed in the C2 aperture holder and the sample is in the sample plane. The most significant advantage of this experimental setup is that it allows to easily change the illumination of the sample. Therefore, it can be used for both the Volta PP, where a focused beam is required, and for the Zernike PP, where a large illuminated area is important. If unspecified, the focused-beam illumination will be considered in the following paragraph. Another advantage of this design is that the sample is placed in a standard sample holder which provides easier replacement than an aperture holder.

The C2 lens creates a crossover close to the objective lens which is then demagnified by the lens and projected onto the sample. Due to the presence of the diffraction grid,

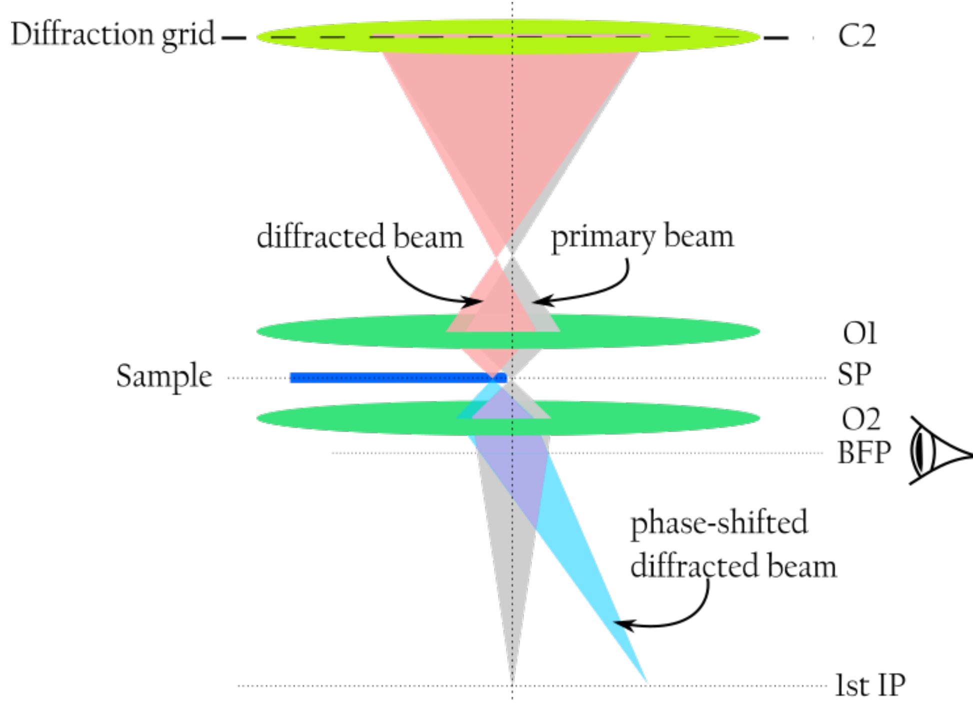

Figure 2.4: Second measurement setup with a diffraction grid in the C2 plane and a sample in the sample plane. The diffraction grid generates diffraction maxima represented by one first-order maximum (red). The maximum passes through the sample (dark blue) and obtains a phase shift. The phase-shifted beam (light blue) interferes with the primary beam (grey) and produces an interference pattern (purple), which is detected (eye mark) in the first image plane.

multiple crossovers are created. For distance L between the C2 lens, the objective lens, distance a' between the C2 lens-produced crossover and the objective lens and small diffraction angles, the crossover spacing D' is approximately equal $D' = (L - a')\lambda/\Lambda$. In the perfect thin-lens optics approximation, the demagnification factor M is determined by the distance a' and the objective focal length f as $M = f/(a' - f)$. The spacing of the image of the crossovers in the sample plane is then given by

$$D \approx f \frac{L - a'}{a' - f} \frac{\lambda}{\Lambda}.$$

Typical values for the distances L and a' are approximately $L \sim 110$ mm and $a' \sim 10$ mm. Therefore, the crossover spacing can be estimated as $D' \sim 8$ m for the finest FIB-prepared grid, and $D' \sim 200$ m for a monocrystal. The listed values are approximately one order greater than the values calculated for the first setup which results in lower requirements on the alignment precision. On the other hand, in the case of a monocrystal, some of the diffraction maxima might get trapped by the microscope column. If the maxima are distant enough, broader electron beam illumination can be used without overlapping of the beams in the sample plane and thus the Zernike PP can be tested. The resulting interference pattern can be then observed in the back focal plane of the objective lens, where the diffractograms corresponding to the individual diffraction orders overlap.

2.1.3. Defocused edge image

In the final design listed, no additional device is needed to perform the measurement. The sample is placed into the sample plane and it is illuminated by a parallel electron beam. Similarly to the previous designs, only half of the illuminated area is covered by the sample. When the optical system is focused properly, a sharp image of the sample is produced in the image plane. However, when changing the objective lens excitation, a diffraction on the sample edge is observable.

In the following, a straight edge of the sample illuminated by a plane wave will be considered. The propagation of the wave behind the sample can be calculated using Huygens-Fresnel principle introduced in section 1.1.2. Let us define a coordinate system in such a way that z points in the direction of the optical axis, and a translucent phase-shifting screen covers the area $x > 0, z = 0$. Let T be the transmissivity of the screen and let ϕ be the phase shift introduced by the screen. Taking the advantage of the symmetry of the defined geometry, the integral in (1.13) can be rewritten as

$$\begin{aligned}\psi(x,y,z) =& \psi_0(x,y,z=0)\frac{1}{2\mathrm{i}\lambda}\frac{\mathrm{e}^{\mathrm{i}kz}}{z}\int_{-\infty}^{\infty}\mathrm{e}^{\mathrm{i}k(y-y_0)^2/2z}\mathrm{d}y_0\cdot\\ &\left[\int_{-\infty}^{0}\mathrm{e}^{\mathrm{i}k(x-x_0)^2/2z}\mathrm{d}x_0 + T\mathrm{e}^{\mathrm{i}\phi}\int_{0}^{\infty}\mathrm{e}^{\mathrm{i}k(x-x_0)^2/2z}\mathrm{d}x_0\right]\end{aligned}$$

As shown in [12], the integrals in the form of $\int_a^b \mathrm{e}^{\mathrm{i}t^2}\mathrm{d}t$ can be expressed in the terms of Fresnel integrals $C(x) := \int_0^x \cos t^2 \mathrm{d}t$ and $S(x) := \int_0^x \sin t^2 \mathrm{d}t$. These odd functions converge to the value of $\frac{1}{2}$ for $x \to \infty$ and $-\frac{1}{2}$ for $x \to -\infty$. After several simplifications, the wave function of a plane wave diffracted by a translucent phase-shifting screen can be expressed as

$$\psi(x,y,z) \propto T\mathrm{e}^{\mathrm{i}\phi}\left[\frac{1}{2}+\frac{\mathrm{i}}{2}+C(x')+\mathrm{i}S(x')\right]+\left[\frac{1}{2}+\frac{\mathrm{i}}{2}-C(x')-\mathrm{i}S(x')\right] \tag{2.2}$$

where $x' = x\sqrt{\frac{k}{2z}}$. The x dependency of the square modulus of the wave function for defocus z =200 µm, transmittance $T = 0.8$ and phase shift $\phi \in \pi \cdot \{0, \frac{1}{4}, \frac{1}{2}, \frac{3}{4}, 1\}$ is shown in Figure 2.5.

2.2. Phase plate effect simulations

Analytical calculations can be done to predict the effect of a phase plate on the electron pattern captured by the camera. The theory needed to describe the effects of the individual optical elements has been presented in 1.1.2. However, in the case of nontrivial geometrical structures such as the structure of the monocrystal or an off-centred phase plate, the integral calculus used within the theoretical description can be very complex and hard to solve. Therefore, numerical computation can be used to get an estimate of the electron intensity distribution.

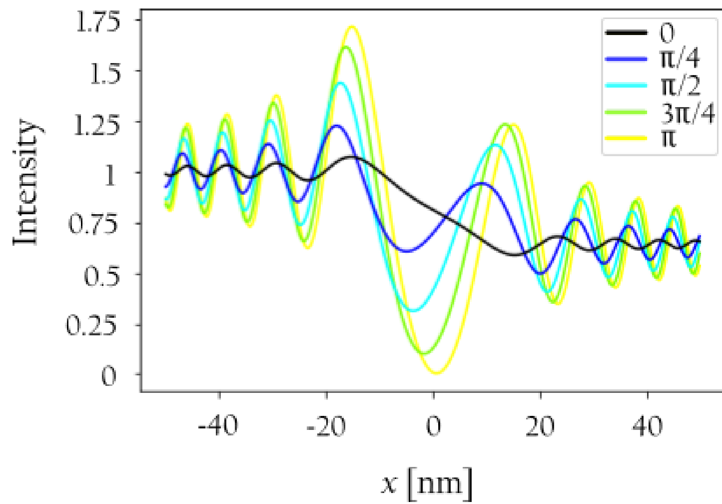

Figure 2.5: Square modulus of the analytical wave function of a plane wave diffracted on an edge of a translucent phase-shifting homogeneous sample.

2.2.1. Diffraction grid simulation

First, let us consider a setup with a diffraction grid producing a set of diffraction maxima on the sample as discussed in 2.1.2. Due to the geometry of the problem, only some of the maxima get phase shifted due to the sample. In the back focal plane of the objective lens, the Fourier transform of the object can be observed. As a result, the set of the diffraction maxima is represented by a superposition of plane waves propagating under different angles.

A squared diffraction in the real space grid can be represented by four maxima laying in the corners of a square in the Fourier space. Those maxima correspond to the diffraction maxima produced by the grid in the sample plane. Let us now consider a phase plate placed in the sample plane in such a way that only two maxima pass through the material. Setting the coordination system in such a way that the maxima would lie on the x and y axis, the wave function in the back focal plane is given as

$$\phi(x, y) \propto \mathrm{e}^{\mathrm{i}kx} + \mathrm{e}^{\mathrm{i}ky} + \mathrm{e}^{\mathrm{i}\phi} \left[\mathrm{e}^{-\mathrm{i}kx} + \mathrm{e}^{-\mathrm{i}ky}\right].$$

The spatial frequency k is determined by the electron wavelength, the distance of the diffraction maxima from the optical axis and by the focal length of the objective lens. However, for the qualitative calculations, the frequency is arbitrary. The simulations were performed on an area of $x, y \in \langle 0, 1\rangle$ arb.units with a wave vector equal to $k = 2\pi/0.2$ arb.units^{-1} and for 21 different phase shifts ranging from 0 to 2π. In Figure 2.6, only the results for phase shifts of 0 and π are shown. The phase shift of the two out of four plane waves resulted in gradual shift of the interference pattern. For the phase shift of π, the pattern moved by half of the period of the grid. Analyzing the shift of the interference pattern between two measurements – one with the sample inserted and one without – the induced phase shift should be obtainable.

In the presented approximative model, the point sources are placed in the front focal plane of the objective lens and perfect plane waves are produced. The superposition of these waves results in a perfect image of the diffraction grid. In a realistic experiment,

however, the sample plane is not identical with the objective front focal plane. As a result, a mixture of real-space image and a diffraction image is produced which corresponds to a defocused image of the grid. The description of such an image is not trivial and the behaviour can vary from the one predicted within this section.

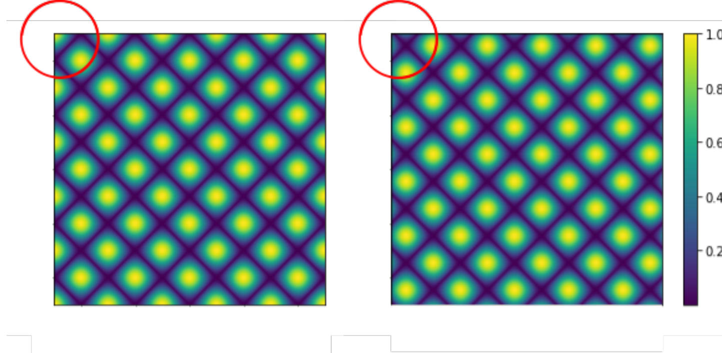

Figure 2.6: The image shift induced by phase-shifting two out of four interfering plane waves. The red circles indicate an area where the images can be compared easily.

2.2.2. Defocused edge simulation

For the simulation of the diffraction on the edge, a simple numerical wave-optics simulation script was created. The script was made in the Python environment and it is based on a set of functions representing the effects of the individual optical elements presented in the experimental setup. In the simulations, a perfect thin lens acting on the electron wave by a phase shift (1.14) is considered. A phase plate induces both a phase-shift and an amplitude drop homogeneously on a defined area. The propagation of the wave between those optical elements is then calculated in the terms of Fourier transform using formula (1.1.2). The individual functions used to describe the effect of the listed optical elements together with an aperture and a diffraction grid (which was not used in the simulations mentioned here) and of the wave propagation are available in the supplementary material.

The numerical simulation procedure of the first setup introduced in Figure 2.7. First, a plane electron wave is limited by a circular aperture to limit the side effects of a rectangular calculation area on the results. After that, the wave propagates by a defined distance onto a phase plate which induces a phase shift and a drop of intensity to a half of the calculation area. The wave then propagates first onto a convex lens which focuses the wave and then to the plane where the image of the aperture is produced. As the phase plate is shifted from the aperture, a defocused image of the plate is produced and diffraction fringes around the edge can be seen. In the simulations, the offset of the phase plate was set to $\Delta z = 200\,\mu\text{m}$, the transmissivity of the plate to $T = 0.75$ and the induced phase shift was varied in the range of $\phi \in \langle 0, \pi \rangle$.

Due to the coordinates-scaling effect of the Fourier transform and a limited computation power, the size of the calculation area was optimized manually to achieve comparable aperture-free areas in the individual computation steps. Best results were achieved for the calculation area of 1.8 µm x 1.8 µm, and thus an aperture of 1.2 µm in diameter. However,

with such settings the diffraction on the aperture is no longer negligible and the resulting intensity profile is significantly modified by this effect. Therefore, a simulation without the phase plate was first performed. The intensity profile obtained for the simulation with the phase plate was then divided by the profile without the phase plate. Please note that the profiles division is not a mathematically correct approach and a deconvolution process is required to obtain more reliable data. On the other hand, this approach is more convenient and gives a sufficient estimate.

The results of the simulations are shown in Figure 2.8. Although the data suffer from noise caused both by limited resolution of the simulations and the incorrect data division, the effect of the phase plate is still clear. However, it does not match with the analytical function introduced in section 2.1.3. In order to achieve a better agreement of the intensity profiles, a computer with higher computational power can be used to increase the computational area and thus reduce the effect of the aperture. Another possibility is to deconvolve the aperture effect, e.g. by a convolution fit of the intensity profile achieved without the phase plate and the analytical function describing the phase plate effect.

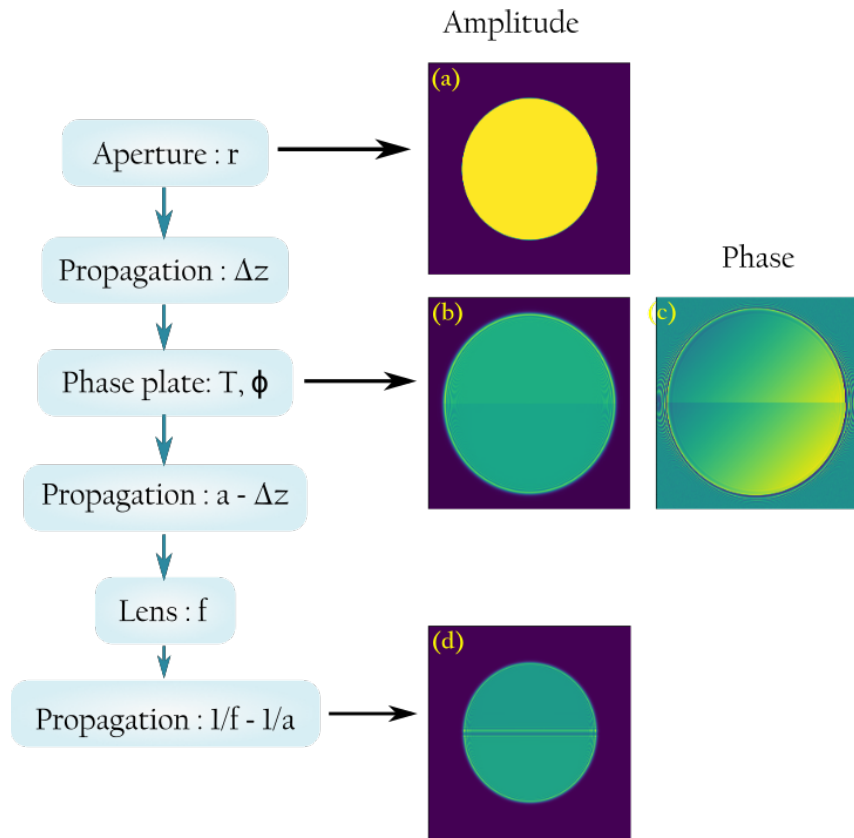

Figure 2.7: Simulation procedure of the defocused-edge measurement. On the left, the sequence of functions used in the simulation is listed. On the right, the wave function amplitudes ((a), (b) and (d)) and phase (c) in significant planes are shown.

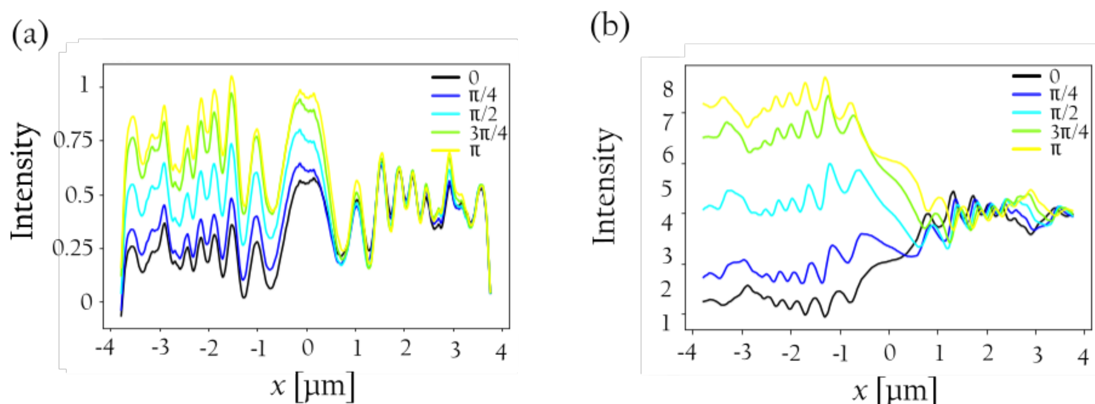

Figure 2.8: Intensity profiles obtained by a numerical simulation of the defocused-edge measurement. (a) Raw simulation results including the effect of the diffraction on the aperture. (b) Intensity profiles devided by a profile of the diffraction on the aperture.

2.3. Experimental setup preparations

Before performing phase shift measurements, the experimental setup has to be prepared. Due to long-term difficulties with the electron biprism delivery, only the experiments with the diffraction grid could be conducted. However, as no spare objective aperture holder nor an SA holder were available during the work on this thesis, only the experimental design of the phase-plate measurement could be tested. As described in section 2.1, the crucial elements of the setup are the diffraction grid and a phase-shifting sample. In the following sections, the preparations of those elements will be described in detail.

2.3.1. Phase plate test samples

For the measurements, silicon nitride (SiN) membranes and silicon dioxide (SiO_2) membranes were chosen as test samples. Both of those materials are available in amorphous form of homogeneous thickness by standard TEM material suppliers. In the experiments, the membranes provided by supplier Agar Scientific Ltd were used – specifically, SiN membranes of thickness 10 nm and 30 nm on a 200 nm Si substrate [72], andSiO_2 membranes of thickness 8 nm, 18 nm and 40 nm on a 200 nm Si substrate [73] were purchased[1]. Unfortunately, the 20 nm thick SiN membrane was damaged during the final measurements, therefore the results presented in section 2.4 do not include this sample. All membranes cover a square substrate-free window and thus in those areas, the samples are transparent for the high-energy electrons in a TEM. The diameter of the substrates is 3.05 mm which corresponds to standard size of TEM samples.

In the designs presented in section 2.1, only half of the electron beam traverses the specimen while the other half passes through vacuum. In order to achieve this effect, a material-free window needs to be fabricated on the samples. For this purpose, a focused ion beam (FIB) lithography can be used. As the title of this technique indicates, a high-energy ion beam is focused on the sample. The collision of the ions with the surface

[1]The samples were purchased from the Thermo Fisher Scientific budget.

of the sample causes sputtering of the surface atoms of the sample and thus milling the material. In conventional FIB devices, two independent guns are present - the FIB gun and an electron gun. Such devices are called dual beam-systems and enable both milling the material with ions and observation of the sample with the secondary electrons generated either by the ion beam or by the electron beam. Due to low energies of the secondary electrons, the information carried by those electrons only comes from the surface of the sample. Since the electron beam is scanned over the sample to produce a complete image, this technique is called scanning electron microscopy (SEM). Within this project, dual beam-systems from the Helios series produced and provided by Thermo Fisher Scientific were used. Those devices include a gallium ion source and the acceleration voltages of both ions and electrons can reach 30 kV [74].

The first tested design of the milling area consisted of a large rectangular window of an area approximately 3 times smaller than the overall size of the substrate-free sample area. This would have enabled convenient manipulation and alignment of the sample in a TEM and it would have ensured that only one half of the electron beam would pass through the material during the phase-shift measurements. However, the membranes could not withstand the large tension caused by the ion beam-milling and were destroyed in the process. In order to reduce tension, a series of varying shapes and sizes of the milled area have been tested. Moreover, the ion beam current and dose have been optimized to limit the risk of membrane breakage.

In the final design, a rectangular area rotated by 45° with respect to the substrate-free window orientation was milled in a corner of a membrane, see Figure 2.9(b). As a result, a triangular material-free window in the corner was created. Using this approach, the membrane retains a convex shape which reduces tension. Furthermore, the choice of rectangular area enables the ion beam to scan in a more effective way which again reduces damage on the sample. The size of the milled area has been optimized to achieve as large a material-free window as possible without destroying the sample. The final size of the hypotenuse of the triangular window is approximately 15 nm. During the milling, an ion beam with current of 2.6 nA was employed. As the Helios systems are widely used for silicon milling in conventional applications, the ion dose is converted into corresponding depth milled into a silicon material in the user interface. To ensure that all material from the membrane would be milled and yet the membrane would not break, a milling depth of approximately 1.5 times the width of the membrane was set. A picture of a sample with a successfully milled window is shown in Figure 2.9(a).

2.3.2. Diffraction grid

As mentioned above, in the chosen design, the diffraction grid has to be inserted into the C2 plane instead of an C2 aperture. A TEM aperture is made of approximately 100 µm thick circular layer of a material of 3.05 mm in diameter (standard size of TEM samples) with a pinhole of varying sizes in the middle. The most widely used apertures are from 50 µm to 200 µm in diameter. An aperture holder contains four aperture slots that have to be filled. The securing mechanism of the aperture is provided by a spring which pushes towards the inner-most aperture. This results in a chain pressure between the apertures and thus fixes the aperture positions. When the holder is inserted to the

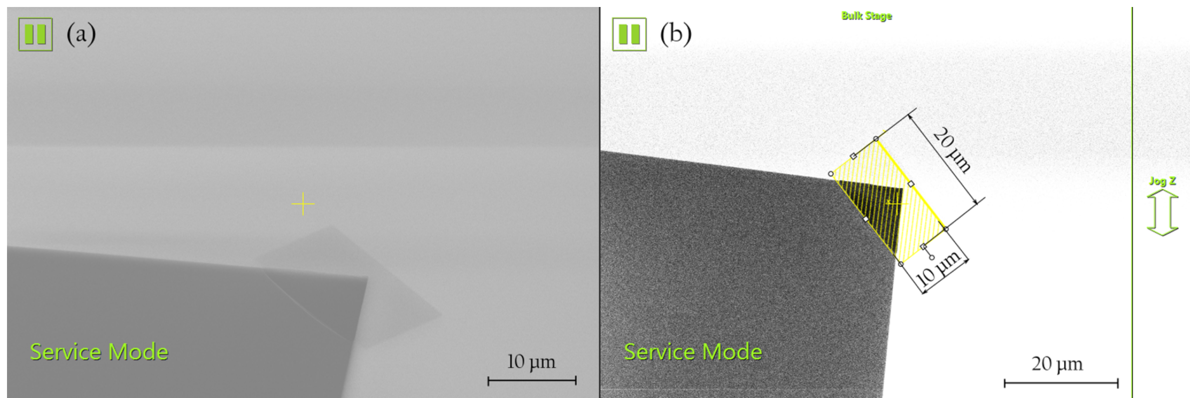

Figure 2.9: A FIB-milled out rectangular area in the corner of a 20 nm thick SiN membrane. (a) SEM picture of a sample tilted by 52° with respect to the electron beam. (b) FIB picture; the yellow rectangle indicates the milling area.

microscope, the switching between the specific apertures and fine position adjustments of the apertures with respect to the optical axis can be done using inner mechanisms. The aperture holder with both conventional apertures and a diffraction sample inserted is shown in Figure 2.10.

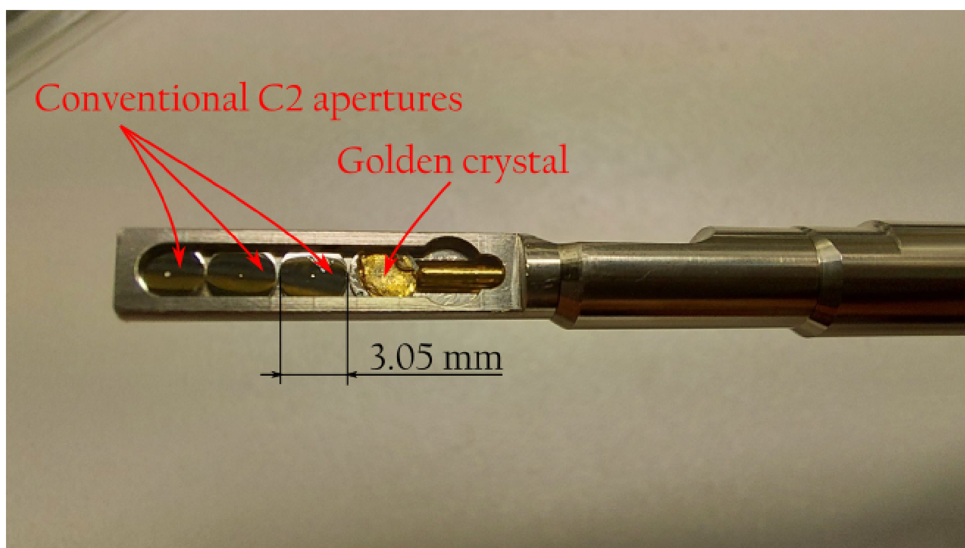

Figure 2.10: C2 aperture holder with three conventional apertures inserted and a an aperture with a gold crystal glued to the top.

For the experiments, two diffraction samples were chosen – a golden crystal [75] and a cross grating [76]. Both samples are placed on a standard copper support grid. As the grid is 20 µm thick, the sample can be put onto a standard C2 aperture. However, due to the combination of a soft and thin support material, the grid can bend easily. Thus, a risk of a release of the grid from the C2 holder in the high vacuum inside the microscope arises. In order to prevent this situation, the samples were glued to an aperture by a thin layer of a vacuum-friendly glue. To ensure that a spot suitable for the diffraction experiment would be available on the area of the pinhole, an aperture with a pinhole of

1000 µm in diameter was used. In Figure 2.11, a SEM picture of the crystal glued to the aperture is shown.

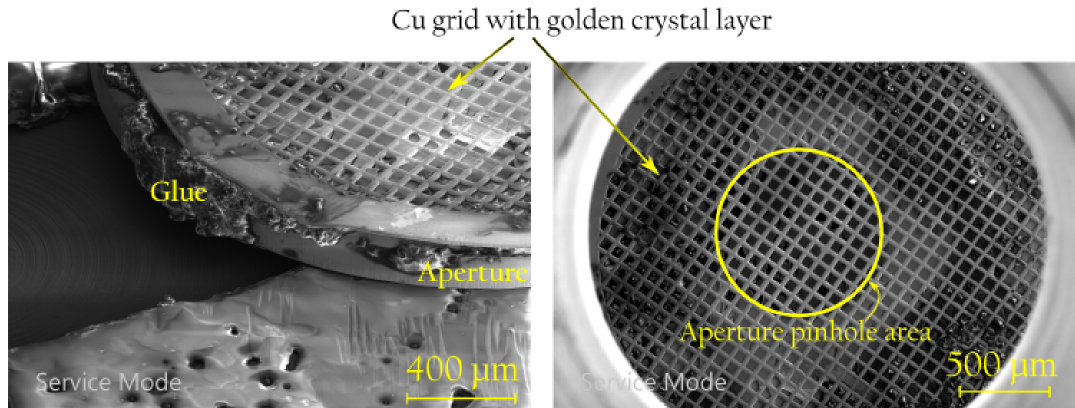

Figure 2.11: SEM images at low magnifications of the gold crystal sample glued to a TEM aperture taken from a side (on the left) and from the top (on the right).

First, the golden crystal was tested. In order to check the diffraction properties, the sample was first inserted into the sample plane of the TEM and observed in the diffraction mode. The diffraction pattern and the corresponding TEM image are visible in Figure 2.12 (a). It is apparent that the sample used consists of areas with different crystal orientations. Hence, in the diffraction pattern, diffraction rings with spots corresponding to dominant crystal orientations are observed. Although the sample is not a monocrystal as considered in the previous chapter, strong diffraction maxima are present in the pattern which can be used within experiment. The crystal was then placed into the C2 aperture holder and inserted into the microscope. However, no diffraction maxima were observed. Due to the demagnification of the C2 lens into the image plane by the objective lens, the propagation angles of the diffraction maxima increased. Assuming a demagnification of $M = 1/50$, the angles increased by a factor of 50. The propagation angle in the image plane of the first diffraction maximum is thus approximately 0.61 rad, which is far from the acceptance angle of a TEM column. As a result, the diffraction maxima get trapped by the column and the sample is not applicable for the experiment.

The cross-grating specimen tested contains 2160 lines per mm in two perpendicular directions, which corresponds to a pattern periodicity of 463.0 nm. This periodicity is approximately 1000 times larger than the one of the golden crystal and thus the diffraction maxima would be 1000 times closer to each other. When the sample is placed into the sample plane, the diffraction effect is not strong enough to be observed in the diffraction mode. However, when the sample was placed into the C2 aperture holder, a clear diffraction pattern can be seen when a single window of the supportive grid was illuminated (see Figure 2.12 (b)). When broadening the electron beam, the diffraction pattern is then modulated by the diffraction on the grid and becomes less clear.

In the experiments, it is advantageous to have as clear diffraction pattern of the cross-grating as possible. Therefore, the illumination area of the C2 aperture needs to be reduced. This can be done by changing the excitations of the optics above the C2 lens, i.e., the electrostatic lens and the C1 lens. However, reducing the illumination by the

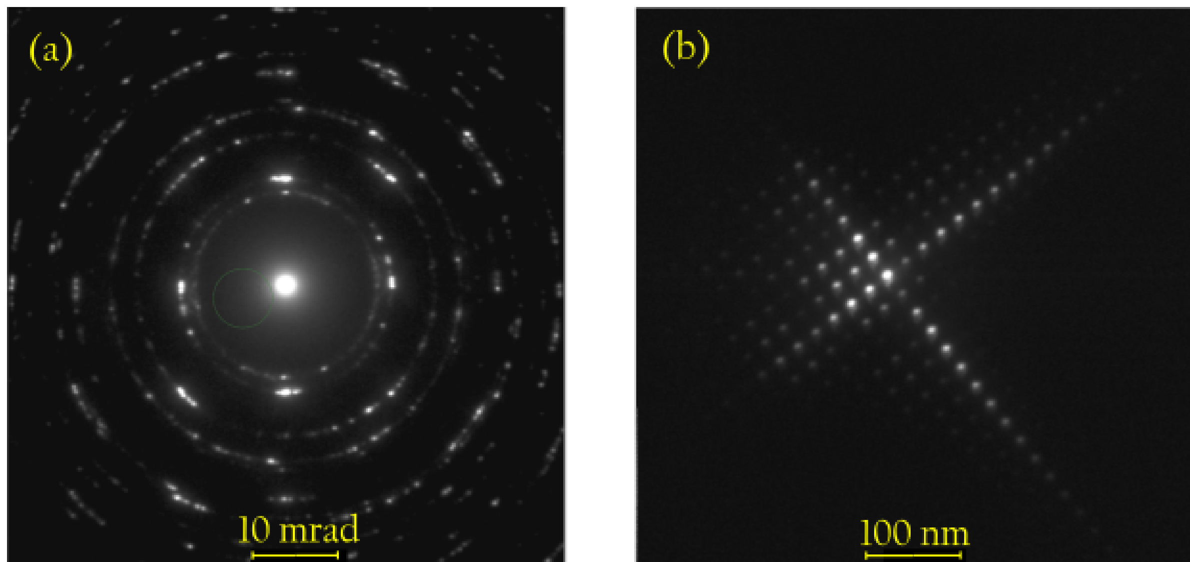

Figure 2.12: The diffraction patterns of the diffraction grid samples. (a) A gold crystal placed in the sample holder and observed in diffraction mode. (b) A cross grating placed in the C2 aperture holder.

C1 lens implies a loss of spatial coherence of the electron beam. As the measurements are based on electron beam interference, the beam coherence is crucial. Therefore, in the experiments, C1 lens was set to achieve the largest illumination while the electrostatic lens was used to reduced the illumination area as much as possible. To test the electron beam coherence, the excitation of the C2 lens was set to illuminate the sample by a slightly defocused beam. Therefore, the neighbouring diffraction maxima overlapped and interfered in the image plane. The presence of the interference pattern is proven by the comparison of the Fourier transform images of the with and without the beam overlapping (see Figure 2.13).

2.4. Phase shift measurement

The measurements were performed on a Talos F200C TEM [77] prototype provided by Thermo Fisher Scientific. This 200 keV device is equipped with a field emission gun and the achievable resolution reaches 0.3 nm. As mentioned above, one standard C2 aperture was replaced with a diffraction sample, while the rest of the C2 apertures remained in the holder. Before each measurement series, the microscope had to be well-adjusted, including alignment of the optical elements, electron beam stigmation and cooling the sample area with liquid nitrogen.

2.4.1. Diffraction grid measurement

In order to ensure that the sample covers approximately half of the field of view, it is first illuminated with a broad electron beam, the objective lens is focused onto the sample and the diffraction grid is retracted. In the TEM user interface, a line can be drawn on

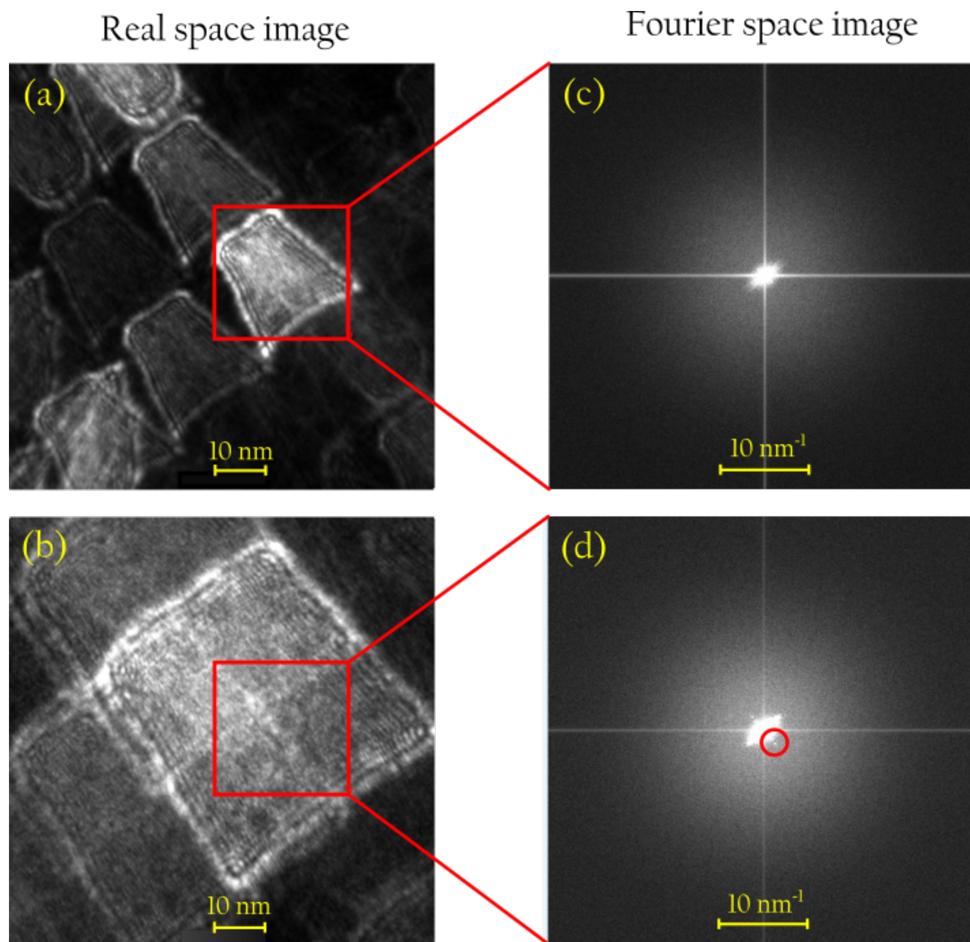

Figure 2.13: Real space images with and without the electron beam overlapping ((a) and (b)) and corresponding Fourier transform images calculated out of the red square-bounded areas ((c) and (d)). In (d), an extra maximum corresponding to the electron beam interference is detected as a proof of the electron beam coherence (marked by the red circle).

the digital screen to mark the edge of the sample in the field of view (see Figure 2.14 (a)). After that, the diffraction grid is inserted into the C2 aperture plane which results in splitting the electron beam into multiple diffraction maxima. The excitation of the C2 lens is then adjusted to focus the electron beams onto the sample plane. Using beam deflectors, the diffraction maxima can be moved to the edge of the sample marked by the line (see Figure 2.14 (b)). Hence, some of the maxima pass through the sample while the rest pass through vacuum. The interference pattern is then observable in the BFP of the objective lens. It is therefore necessary to switch from imaging mode to diffraction mode in further measurements.

As predicted in the simulations (see section 2.2.1), a defocused image of the diffraction grid is produced in the BFP. In order to determine the effect of the sample on the image in the BFP, a pair of pictures has to be taken – one with and one without the sample. Within the experiment, multiple measurements were performed for each specimen. The original sample position with the edge placed in the middle of the field of view, as well as

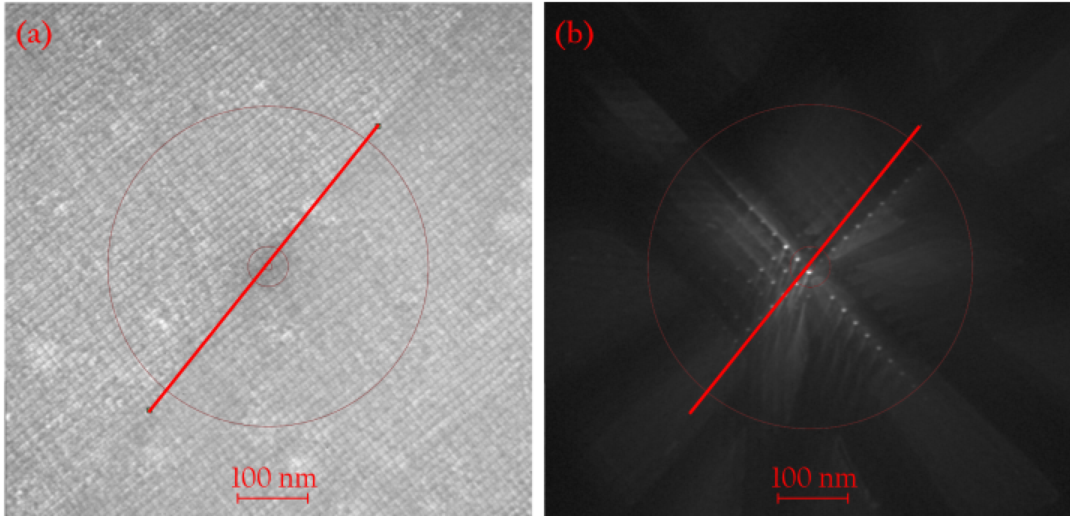

Figure 2.14: The edge (red line) of a 40 nm thick SiO_2 membrane illuminated by (a) a broad and (b) a focused electron beam with a diffraction grid inserted in the C2 plane.

a position without the sample, was saved in the TEM user interface. In each measurement step, the sample position was set to one of these values and a picture was captured.

The comparison of the two interference patterns in the BFP is shown in Figure 2.15 (a) and (b). As can be seen, the presence of the sample results in the spatial shift of the interference pattern. This is in accordance with the results of the simulations. Due to the periodicity of the grid, the quantitative analysis of the shift might be ambiguous. However, unlike in the simulation, the shifting pattern includes irregular features corresponding to impurities on the sample. Hence, the shift of those features can be quantified in order to determine the effect of the sample.

The origin of the sample-induced shift of the interference pattern is illustrated in Figure 2.16. Let us neglect the curvature of the electron wavefront in the BFP so the interference pattern can be estimated by a superposition of plane waves, where the tilt of the wave propagation with respect to the optical axis corresponds to individual diffraction maxima. In the figure, only the primary beam and first diffraction maxima propagating by an angle θ are shown. The crossovers of the wavefronts denote the position of the interference maxima. The phase shift $\Delta\phi$ of the diffracted wave results in a lateral shift of the maxima Δx. In this approximation, the lateral shift is thus given by $\Delta x = \Delta\phi/(k \sin\theta)$, where k is the wavenumber.

In order to determine the phase shift of an electron wave induced by the specimen, the shift of the interference pattern has to be analyzed. As mentioned above, it is beneficial to track the movement of impurities on the diffraction grid. The image of the grid itself can be filtered out using a low-pass frequency filter. Hence, only the low-frequency information of the image would be further analyzed. The shift of the filtered image can be then obtained using two methods. In the first one, points of maximum intensity are found in the two images and the shift is determined by the distance between those points. Although this method can easily collapse when multiple high-intensity features appear

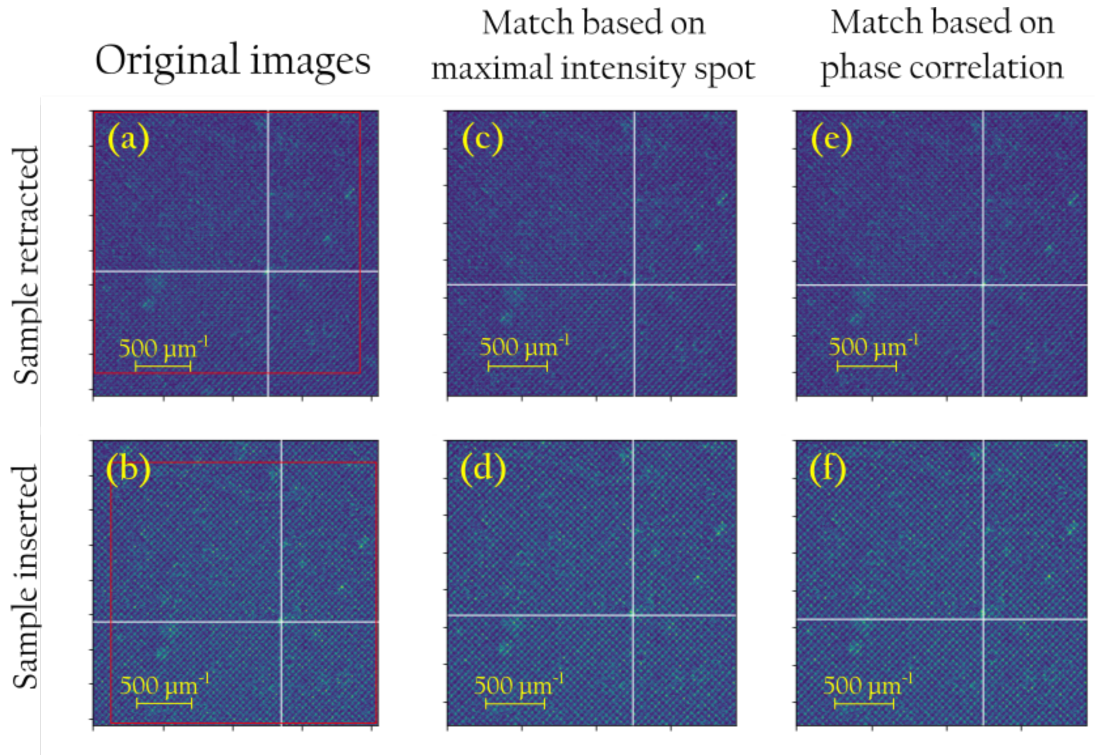

Figure 2.15: Interference patterns detected in the back focal plane with a diffraction grid in the C2 plane and (a) with and (b) without a 40 nm thick SiO_2 membrane inserted in the sample plane. The white crosses indicate a position of a feature that can be tracked to compare the images. The red rectangle shows the approximate area the two images have in common. The common areas are identified by the maximal intensity detection ((c) and (d)) and phase correlation ((e) and (f)).

in the images, it does not need much of computational power and it works considerably well for most of the measurements. In the second method, a phase correlation of the two images is calculated and the shift is then determined by the position of the maximum of the correlation function. In Figure 2.15 an example of results of the image matching based on both the intensity maximum detection and the phase correlation is shown. Although none of the matching techniques is perfect, they provide sufficient and comparable results. The image shifts determined by the techniques for all of the measurement series are summarized in Figure 2.17.

Comparing the image shift results achieved for individual samples, the uncertainity of the measurement can be achieved, see Table 2.1 and Figure 2.18. As the induced phase shift is proportional to the product of the sample thickness and the mean inner potential of the material, a linear dependence of the image shift on the sample thickness was expected. However, the measurement results obtained for the SiO_2 samples do not show an agreement with the expectations a the image shift induced by a 18 nm thick membrane exceeds the shift induced by a 40 nm thick membrane. Moreover, only a negligible image shift is achieved in most of the measurements of a 30 nm thick SiN membrane.

The obtained results might be negatively affected by the instabilities of the electron-sample alignment, since both the electron beam and the sample could have drifted during

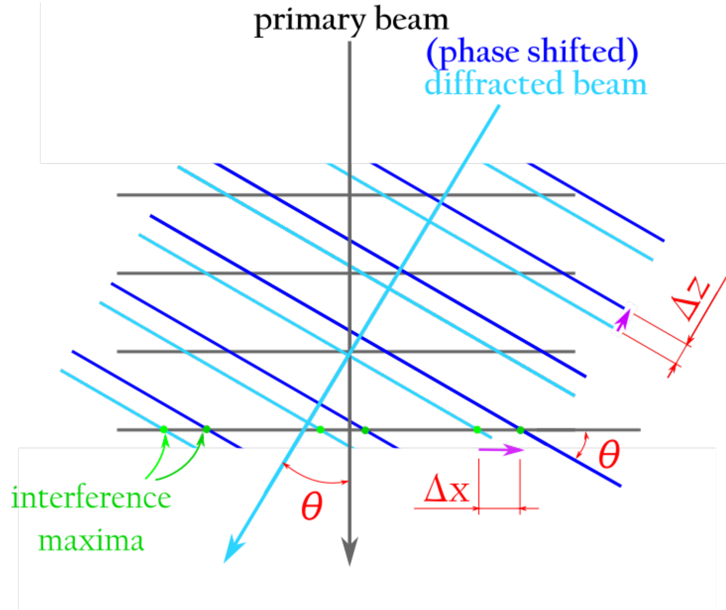

Figure 2.16: Lateral shift Δx of the interference pattern caused by phase shift $\Delta\phi = k\Delta z$ of the diffracted beam propagating under angle θ.

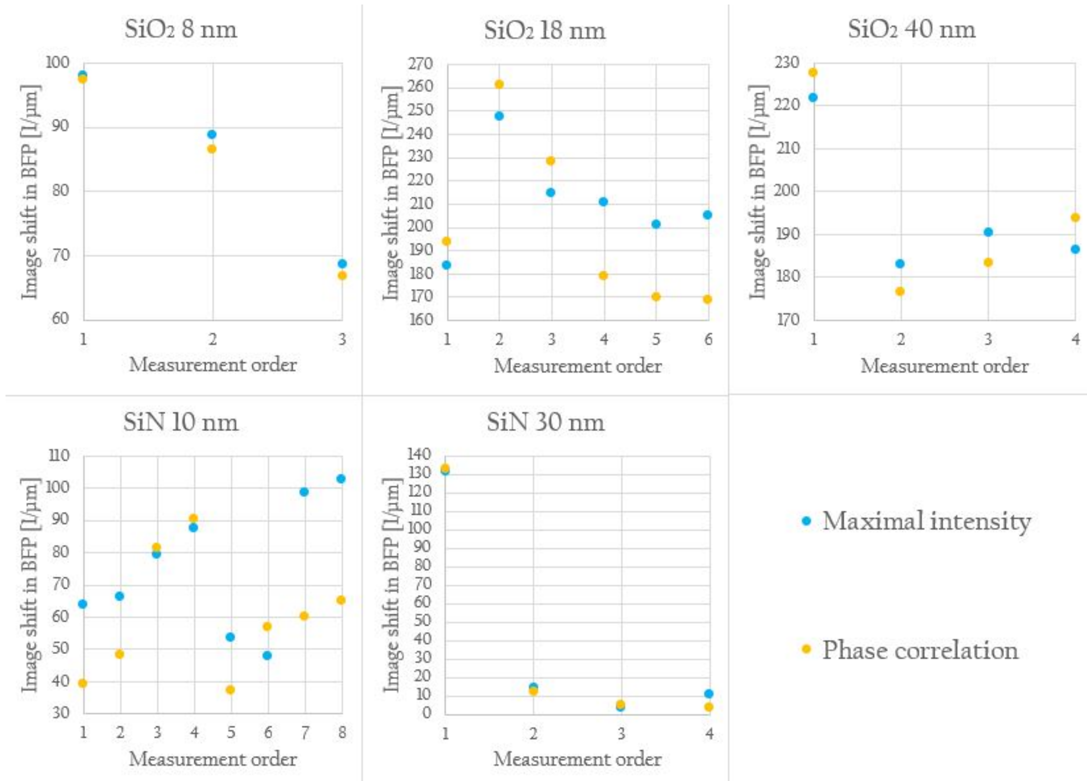

Figure 2.17: Quantitative image shift results obtained by the maximal intensity detection (blue dots) and phase correlation (yellow dots).

the measurements. Due to relatively small spacing of the diffraction maxima on the sample, even a small drift can influence the measurement significantly as different number of the maxima would traverse the sample. The reliability of the sample position adjust-

Table 2.1: Average values of the image shift obtained for individual samples.

SiO_2 8 nm	SiO_2 18 nm	SiO_2 40 nm
(84 ± 14) µm^{-1}	(205 ± 19) µm^{-1}	(195 ± 16) µm^{-1}

SiN 10 nm	SiN 30 nm
(68 ± 12) µm^{-1}	(40 ± 50) µm^{-1}

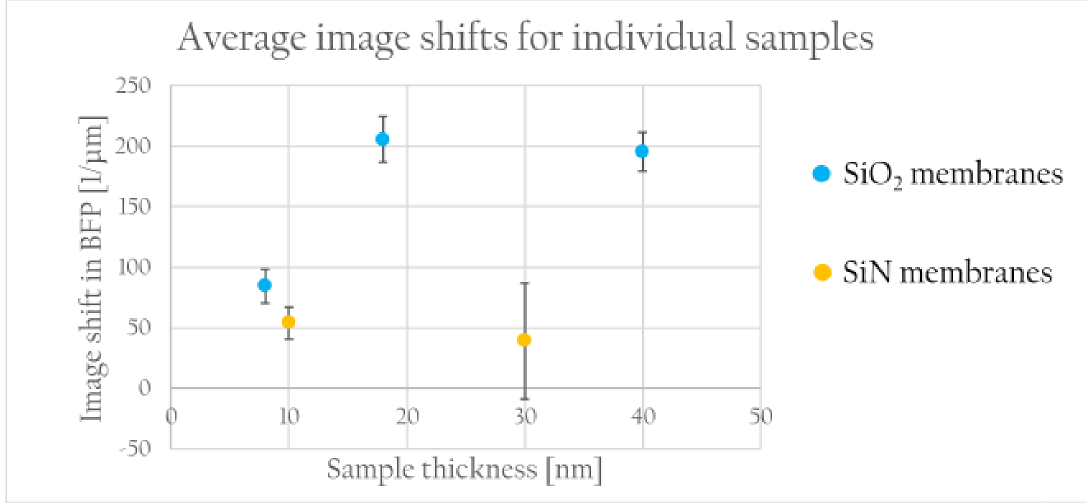

Figure 2.18: Average values of the image shift obtained for individual samples.

ment was tested before the measurement itself. It was found that for a sample movement in directions perpendicular to the electron beam, a movement in one direction provides strong uncertainty, whereas in the other direction, the sample position can be adjusted with an uncertainty of approximately 5 nm. Therefore, the sample was only moved in this direction during the measurements.

The instability of the electron beam is illustrated in Figure 2.19, where a picture of the position of the focused electron beam with respect to the sample edge (red line) was captured both before and after a measurement series. The drift of the electron beam can be caused by temperature instability. Another possible explanation is a beam-induced charging of the sample. This effect can be very significant as the beam illuminates the edge of the sample where charge can accumulate.

2.4.2. Defocused edge measurement

In this measurement, the sample is illuminated by a parallel electron beam and the objective lens is focused into a plane above or below the specimen, as described above. Again, the sample is placed in such a way that it only covers half of the illuminated area. This results in diffraction of the electron beam on the edge of the specimen and production of diffraction fringes described by (2.2). In the measurements, a conventional C2 aperture of 150 µm was used. A parallel illumination of the sample is provided when the electron beam is focused in the back focal plane of the objective lens. This can be achieved by

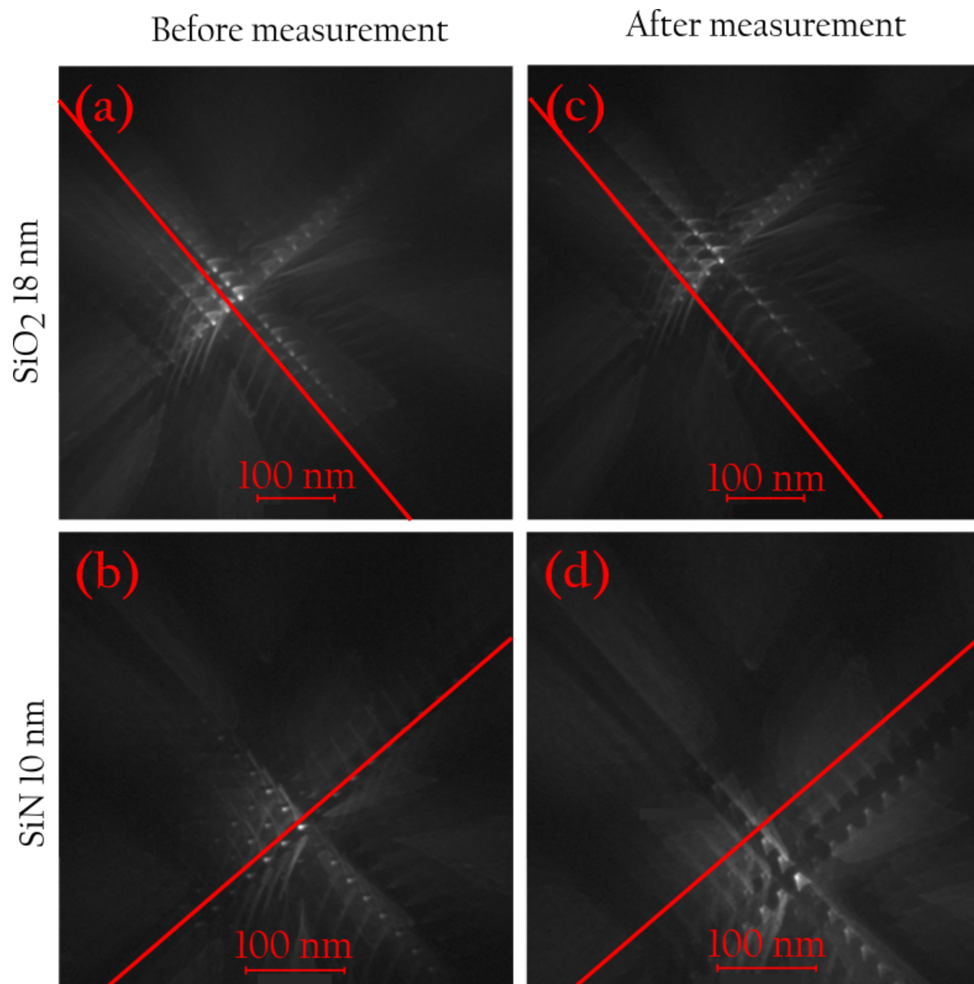

Figure 2.19: Drift of the diffraction pattern produced by a diffraction grid in the C2 plane – relative position of the pattern with respect to the edge of the sample (red line) before ((a) and (b)) and after ((c) and (d)) after the measurement series.

correctly setting the C2 lens excitation. In order to create a focused image in the image plane, the longitudinal position of the sample was first adjusted to obtain rough imaging settings and then the objective lens excitation was changed to achieve a perfect focus. The TEM user interface includes a conversion of the objective lens excitation to a longitudinal position of the in-focus plane with respect to a reference plane.

For each specimen, a series of measurements was performed. In each measurement step, the objective lens excitation was changed to obtain a defocus of 10, 20, 30, 40, 50, 100, 150 and 200 μm and pictures of the sample edge were recorded on a built-in high quality camera. In Figure 2.20, a series of measurements on a 30 nm thick SiN sample is shown. The 1D cross-sections were obtained after processing the original data according to the procedure shown in Figure 2.22. It is clear that for increasing defocus, the diffraction fringes are more and more visible and they reach further from the sample edge. In Figure 2.21, a comparison of diffraction fringes at the edges of different samples obtained at the same defocus can be seen. The diffraction fringes of SiN membranes have considerably better contrast and "sharpness" than the fringes on SiO_2. This is probably caused by low homogenity of the SiO_2 samples as can be seen in Figure 2.23.

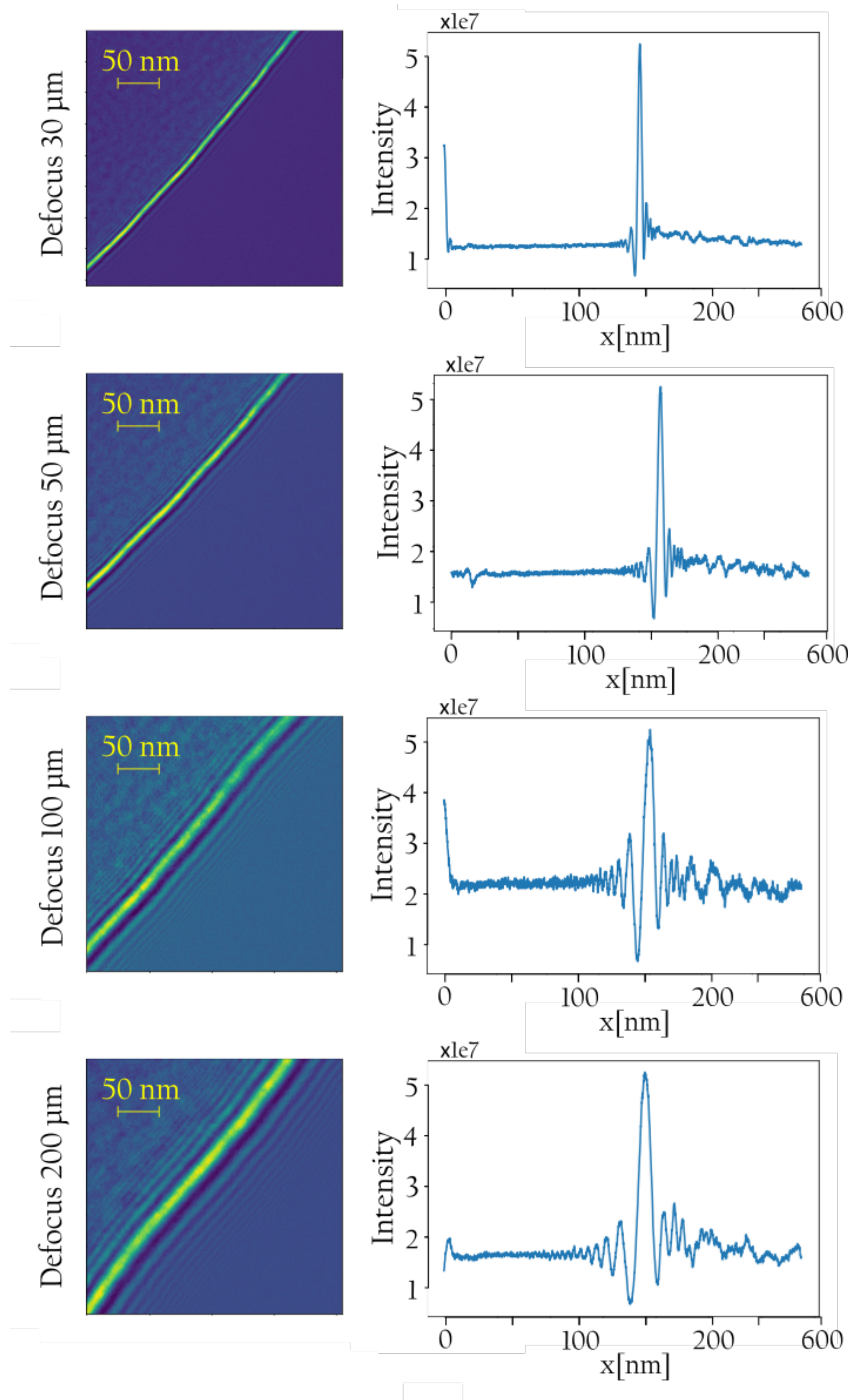

Figure 2.20: Measurement series for an 18 nm thick SiO_2 membrane – 2D and 1D intensity profiles for a different defocus.

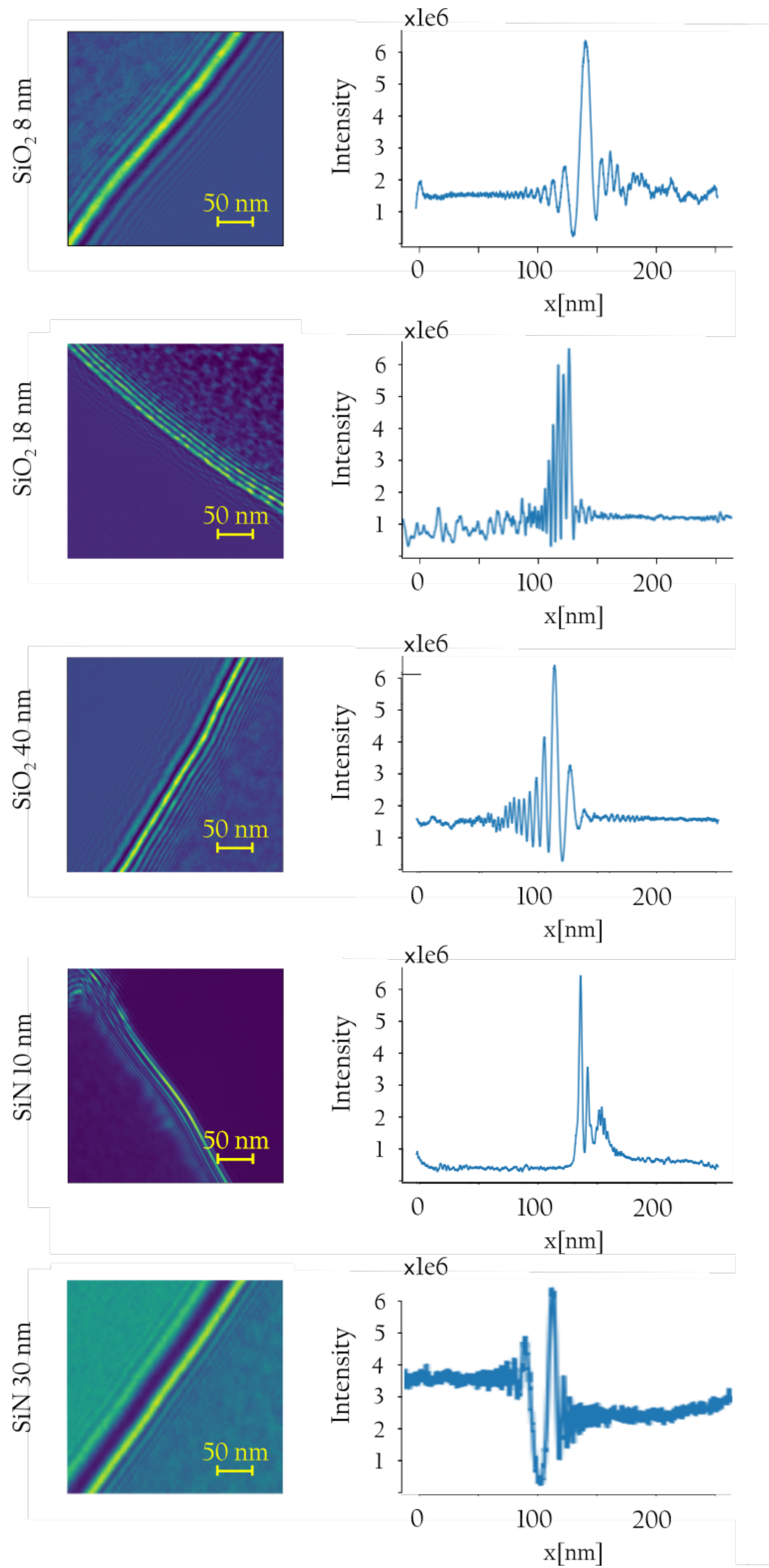

Figure 2.21: Measurements at 200 μm defocus for different samples – 2D and 1D intensity profiles for a different defocus.

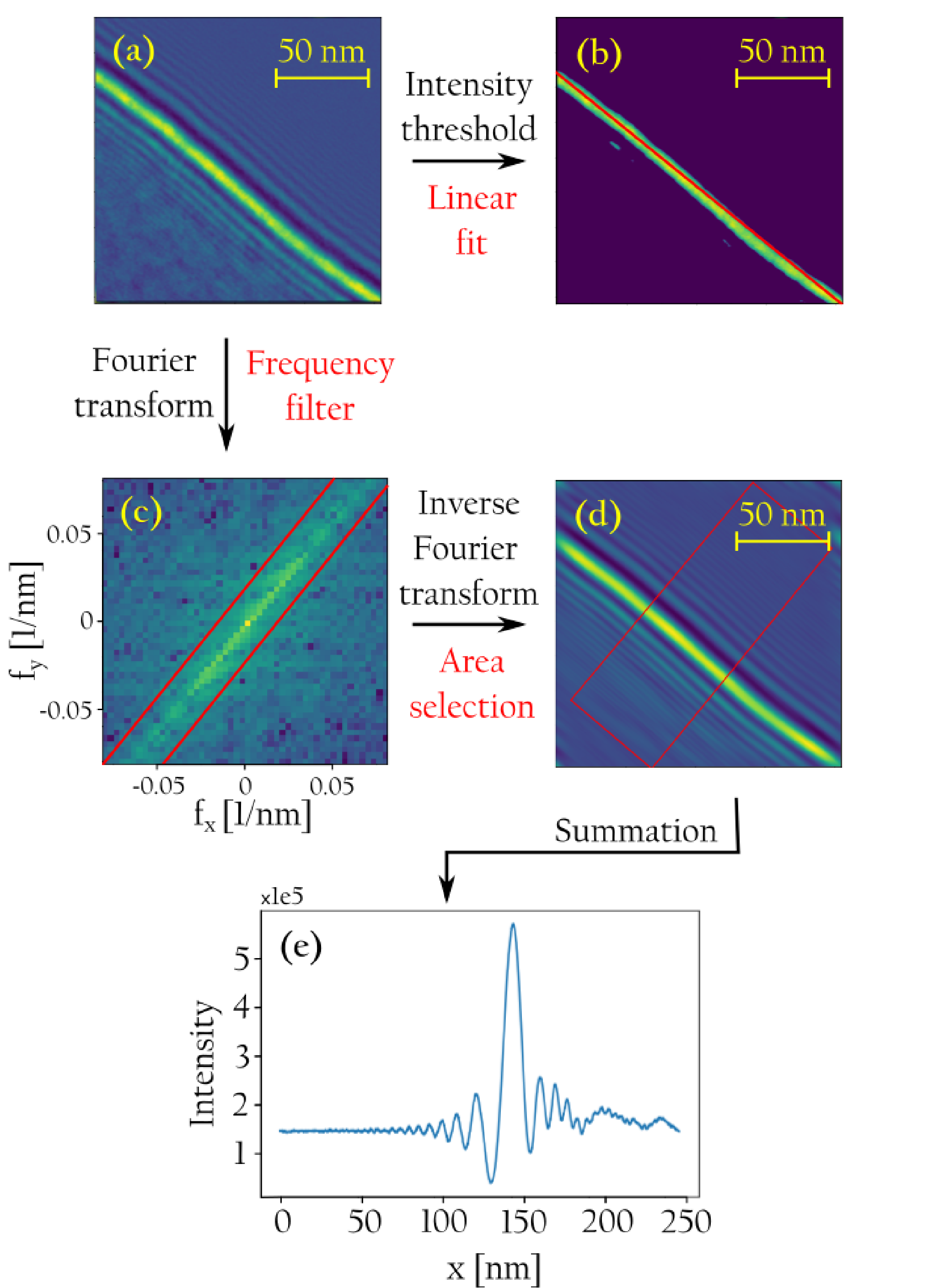

Figure 2.22: Image processing procedure to obtain the intensity profile of the measured diffraction fringes (a). The orientation of the fringes is determined by intensity thresholding of the measured data and fitting the result with a linear function (red line in (b)). Then, a narrow intensity stripe in the direction perpendicular to the fringes is selected (between the two red lines in (c)) and the intensity at the remaining frequencies is set to zero to reduce the noise in the image. An inverse Fourier transform image is obtained from the modified spectra and a rectangular area in the direction perpendicular to the fringes is selected (red rectangle in (d)). Finally, the intensity is summed over the shorter side of the rectangle and one dimensional intensity profile is achieved (e).

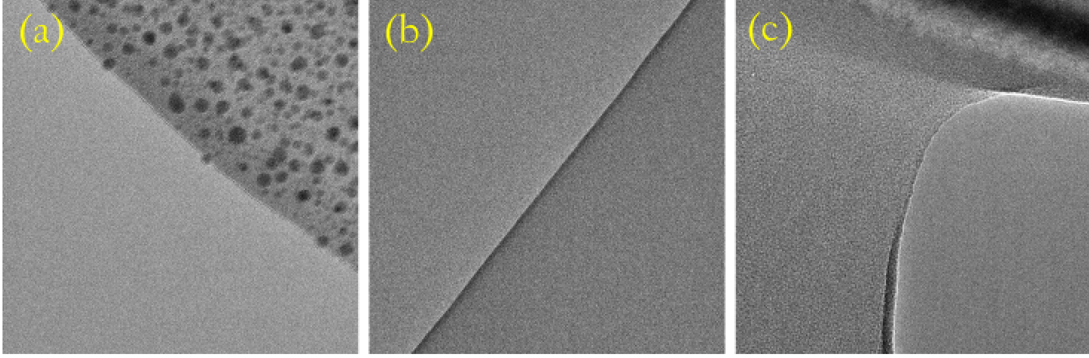

Figure 2.23: Imperfections of the samples. (a) Inhomogeneities of the 18 nm thick SiO_2 layer and a rough sample edge. (b) Higher contrast at the edge of a 30 nm thick SiN membrane. (c) Folded edge of a 10 nm thick SiN membrane in the bottom of the image.

The theory introduced in section 2.1.3 predicts that the shape of the diffraction pattern profile depends on the transmissivity of the layer, the induced phase shift and the distance from the layer (defocus). The transmissivity determines a ratio of intensities towards the diffraction pattern convergencies for $x \to \infty$ and $x \to -\infty$, and the defocus determines the fringes periodicity. The steepness of intensity profile only depends on the induced phase shift. Fitting the measured profile with the analytical function (2.2) should thus lead directly to the individual parameters including the phase shift. In order to obtain the best matching between the measured profile and the fit, linear scaling of both the x and y axis has to be taken into account, which results in four more fitting parameters.

A least square-method fitting was performed in Python environment using library *lmfit*. The boundaries of the individual fitting parameters were limited to reduce the degrees of freedom of the fit and the specific boundary values were optimized manually to obtain the best fit possible. However, no satisfactory fit was achieved for any data set. Moreover, multiple combinations of the fitting parameters providing similar results were found. As the analytical function considers a perfectly coherent beam, the disagreement of the measured data and the fitting function might be caused by the lack of coherence of the electron beam. The partial spatial coherence A can be described as a function of spatial frequencies q

$$A(q) \propto e^{-\frac{\beta^2}{4\lambda^2}\left|\frac{\partial\gamma(q)}{\partial q}\right|^2}, \tag{2.3}$$

where β is the angle-distribution parameter, λ is the electron wavelength and $\gamma(q)$ is the aberration effect of the contrast transfer function described in (1.20) [78]. The aberration term includes the contribution of the spherical aberration and the defocus. As the measurements were performed in large defocus, the effect on the spatial coherence might be remarkable. The defocus term is proportional to q^2, the resulting partial spatial coherence is given by $A(q) \propto \mathrm{e}^{-\alpha' \mathrm{q}^2}$, where α' is a parameter describing the effect of the defocus. The spatial coherence function acts on the frequency image of the diffraction pattern which corresponds to the Fourier transform of the real-space image. The effect on the real-space image I is thus given by

$$I'(x) \propto I(x) * \mathrm{e}^{-\alpha x^2}, \tag{2.4}$$

where $\alpha = 1/\alpha'$. The fitting function was thus modified to cover the partial coherence effect. The coherence function results in attenuation of the fringes away from the edge

which provides better agreement with the measured profiles. However, in the area of the edge, the disagreement of the measured and fitted profiles is still remarkable. Thus, the fit of the data was not successful. The best achievable fit is shown in Figure 2.24.

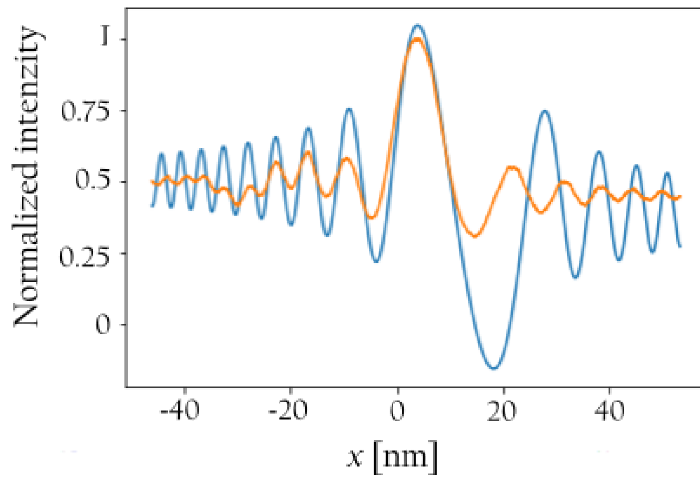

Figure 2.24: The best achievable fit (blue curve) of a measured intensity profile (orange curve) of a 8 nm thick SiO_2 membrane. Fit parameters: Transmitivity $T = 0.98$, phase shift $\phi = -0.40$ rad.

The fit failure might be caused by inhomogeneities of the material which were not considered in the fitting function. The sample imperfections might origin from impurities and contamination on the sample surface (see Figure 2.23 (a)). An electron-beam induced charge could have accumulated around the edge of the sample resulting in non-homogeneous charge density acting on the electron beam. As the FIB-milled sample edge is not perfectly straight, a nontrivial diffraction pattern might have been produced. Therefore, the summation of the intensity over a broad area in the direction of the fringes (as shown in Figure 2.22 (d)) might result in data distortion. The most significant effect, however, is that the material properties have been locally modified around the sample edge by the FIB. In Figure 2.23 (b), different contrast at the edge of the sample can be seen. The most likely explanation is redeposition of material on the sample edge during the FIB milling, resulting in a larger sample thickness around the edge. Therefore, the sample-induced electron beam phase shift differs with respect to the distance from the edge. Furthermore, the edge of the sample then tends to fold on itself, see Figure 2.23(c). In order to obtain better agreement of the measured data with the analytical function, a finer sample preparation method should be used. Moreover, the edge-charging effect could be included in the analytical function.

Conclusions

This Master's thesis aimed to give an overview of phase plate principles and to design an implementation of a chosen phase plate into a transmission electron microscope. The first goal was met within the first chapter of the thesis. Here, the physical principles and various specific designs of thin film-based phase plates together with electrostatic and magnetic phase plates are discussed in detail. The only commercially used phase plates are Zernike phase plate and Volta phase plate which are both based on a thin layer of amorphous carbon. As no further research has been done regarding suitable materials for these phase plate designs, a measurement design enabling the testing of phase-shifting properties of other materials became the main scope of the thesis. In the second chapter, four different measurement designs suitable for implementation into TEMs of Talos series have been introduced. Two of the designs have been tested experimentally and simulated numerically using Python scripts developed within the scope of this thesis.

The first tested measurement design takes the advantage of a diffraction grid placed in the C2 aperture holder. As the diffraction maxima created on a golden crystal, which was originally chosen as the diffraction structure, got trapped by apertures inside the microscope column, the measurements were performed with a conventional cross grating sample. Due to small spacing of the produced diffraction pattern, however, the setup was very sensitive to electron beam-sample alignment resulting in a great instability of the measurements. In order to enhance the robustness of the measurement design, a diffraction grid with smaller parameter could be used. An ideal grid would then create strong first-order maxima that would be able to propagate through the microscope column, while the rest of the maxima would get trapped. Besides the enhanced stability of such a design, the reduced diffraction pattern would allow more straightforward data interpretation. Another possibility would be to use the first diffraction grid-based design introduced in the thesis, where the grid is placed into the sample plane while the sample is in the back focal plane of the objective lens. As this design provides different magnification factors, the golden crystal can be used for the measurement. However, the polycrystalline structure results in nontrivial diffraction pattern resulting in much more complex interference pattern produced by the optical setup and thus more complicated data interpretation.

In the second measurement design tested within this thesis, a defocused image of the sample edge was captured. The analytical function describing the resulting intensity profile, however, did not correspond to the measured data. In order to overcome this problem, a more complex analytical function including the effects of charging around the

sample edge should be used. Moreover, a finer sample preparation technique could be adapted to create a sharper and more homogeneous edge of the sample.

Although the two presented unconventional phase shift measurements have not produced relevant phase-shift results yet, the improvements mentioned in the paragraphs above can lead to successful measurements. More accurate results can be derived using a conventional electron biprism. Although this technique was also discussed within this thesis, the device was not available during the work on the project and thus the results could not be compared to the other presented techniques. However, due to greater accessibility and lower costs of the other measurement designs, they can be implemented in laboratories more easily and provide a convenient way of the phase-shift measurement. Although the defocus-based measurement is only applicable on the thin film phase plates, the diffraction structure also provides the application possibility for the other phase plates designs.

Bibliography

[1] Nion Company. *Products: The UltraSTEM range.* [online, cited on 2022, May 19] https://www.nion.com/products.html.

[2] O.L. Křivánek, T.C Lovejoy, N. Dellby. *Aberration-corrected STEM for atomic-resolution imaging and analysis.* In: Journal of Microscopy, 259(3), pp. 165-172 (2005). https://doi.org/10.1111/jmi.12254.

[3] J. Gonnissen, A. De Backer, A.J. den Dekker, et al. *Atom-counting in High Resolution Electron Microscopy:TEM or STEM - That's the question.* In: Ultramicroscopy, 174, pp. 112-120 (2017). https://doi.org/10.1016/j.ultramic.2016.10.011.

[4] M. Tanaka. *Glossary of TEM Terms.* JEOL Ltd. [online, cited on 2022, May 19] https://www.jeol.co.jp/en/words/emterms/search_result.html?keyword=.

[5] L. Reimer and H. Kohl. *Transmission Electron Microscopy (Fifth Edition).* Springer, 2008. ISBN 978-0-387-40093-8.

[6] D.B. Williams and C.B. Carter. *Transmission Electron Microscopy.* Springer, 2009. ISBN 978-0-387-76500-6.

[7] M. Karlík. *Úvod do transmisní elektronové mikroskopie.* Česká technika, 2011. ISBN 978-80-01-04729-3.

[8] P. Dub, J. Spousta and J.Zlámal. *Kvantová mechanika.* Institute of Physical Engineering BUT, 2015. [online, cited on 2022, May 19] http://www.physics.fme.vutbr.cz/files/opory/pdf/QM/QM.pdf.

[9] L.D. Landau and E. M. Lifshitz, *Quantum Mechanics Non-relativistic Theory (Third Edition).* Pergamon Press Ltd., 1965. ISBN 0-08-020940-8.

[10] L.I. Schiff. *Quantum Mechanics.* McGraw-Hill Book Company, Inc., 1949. ISBN 9780070702431.

[11] Y.B. Band and Y. Avishai. *Quantum Mechanics with Applications to Nanotechnology and Information Science.* Academic Press, 2013. ISBN 978-0-444-53786-7.

[12] J. Komrska. *Vlnová optika - Difrakce světla.* Akademické nakladatelství CERM, 2004. ISBN 80-214-2822-8.

[13] H. Shinotsuka, S. Tanuma, C.J. Powell and D.R.Penn *Calculations of electron inelastic mean free paths. X. Data for 41 elemental solids over the 50eV to 200keV range with the relativistic full Penn algorithm.* In: Surface and Interface Analysis, 47(9), pp. 871-888 (2015). https://doi.org/10.1002/sia.5789.

[14] P. Zhang, Z. Wang, J.H. Perepezko and P.M. Voyles. *Elastic and inelastic mean free paths of 200 keV electrons in metallic glasses.* In: Ultramicroscopy, 117, pp. 89-95 (2016). https://doi.org/10.1016/j.ultramic.2016.09.005.

[15] D. Jannis, K. Müller-Caspary, A. Béché and J. Verbeeck. *Coincidence Detection of EELS and EDX Spectral Events in the Electron Microscope.* In: Applied Sciences, 11(9058), (2020). https://doi.org/10.3390/app11199058.

[16] J. Garcia de Abajo. *Optical excitations in electron microscopy.* Review of Modern Physics, 82(1), pp. 209-275 (2010). https://doi.org/10.1103/RevModPhys.82.209.

[17] Thermo Fisher Scientific Inc. *Transmission Electron Microscopy vs Scanning Electron Microscopy.* [online, cited on 2022, May 19] https://www.thermofisher.com/cz/en/home/materials-science/learning-center/applications/sem-tem-difference.html.

[18] P.W. Hawkes, *Charged-Particle Optics.* In: Encyclopedia of Physical Science and Technology. Academic Press, 2003, pp. 667-696. https://doi.org/10.1016/B0-12-227410-5/00095-8.

[19] Practical Electron Microscopy and Database. *Helical Trajectory/Image Rotation Inversion in Magnetic Fields.* [online, cited on 2022, May 19] https://www.globalsino.com/EM/page4903.html.

[20] S. Amelinckx, J. Van Landuyt *Transmission Electron Microscopy.* In: *Encyclopedia of Physical Science and Technology.* Academic Press, 2003, pp. 53-87. https://doi.org/10.1016/B0-12-227410-5/00789-4.

[21] O. Scherzer. *Über einige Fehler von Elektronenlinsen.* In: Zeitschrift für Physik, 101, pp. 593-603 (1936). https://doi.org/10.1007/BF01349606.

[22] Thermo Fisher Scientific Inc. *Spectra 200 TEM.* [online, cited on 2022, May 19] https://www.thermofisher.com/cz/en/home/electron-microscopy/products/transmission-electron-microscopes/spectra-200-tem.html.

[23] P. Batson. *Sub-Ångstrom Resolution Using Aberration Corrected Electron Optics.* In: Nature, 418(6898), pp. 617-20 (2002). https://doi.org/10.1038/nature00972.

[24] J. Rodenburg. *Learn to use TEM.* [online, cited on 2022, May 19] http://www.rodenburg.org/guide/t1100.html.

[25] J. Bednár. *"Chladná" moderní elektronová mikroskopie.* In: Pokroky matematiky, fyziky a astronomie, 62(4), pp. 237-253 (2017). ISSN: 0032-2423.

[26] H.P. Erickson and A. Klug. *Measurement and compensation of defocusing and aberrations by Fourier processing of electron micrographs.* In: Philosophical Transactions of the Royal Society of London B, 261(837), pp. 105-118 (1971). https://doi.org/10.1098/rstb.1971.0040.

[27] O. Scherzer. *The Theoretical Resolution Limit of the Electron Microscope.* In: Journal of Applied Physics, 20, pp. 20-29 (1949). https://doi.org/10.1063/1.1698233.

[28] Thermo Fisher Scientific Inc. *Phase Plate.* [online, cited on 2022, May 19] https://www.fei.com/products/phase-plate/#gsc.tab=0.

[29] A. Sánchez and M.A. Ochando. *Calculation of the mean inner potential.* In: Journal of Physics C: Solid State Physics, 18, pp. 33-41 (1985). https://doi.org/10.1088/0022-3719/18/1/011.

[30] P. Kruse, M. Schowalter, D. Lamoen, et al. *Determination of the mean inner potential in III–V semiconductors, Si and Ge by density functional theory and electron holography.* In: Ultramicroscopy, 106, pp. 105-113 (2006). https://doi.org/10.1016/j.ultramic.2005.06.057.

[31] R. Danev, K. Nagayama. *Transmission electron microscopy with Zernike phase plate.* In: Ultramicroscopy, 88, pp. 243-252 (2001). https://doi.org/10.1016/S0304-3991(01)00088-2.

[32] M. Marko, X. Meng, X. Hsieh, et al. *Methods for testing Zernike phase plates and a report on silicon-based phase plates with reduced charging and improved ageing characteristics.* In: Journal of Structural Biology, 184, pp. 237-244 (2013). http://dx.doi.org/10.1016/j.jsb.2013.08.008.

[33] F. Zernike. *Diffraction Theory of the Knife-Edge Test and its Improved Form, the Phase-Contrast Method.* In: Monthly Notices of the Royal Astronomical Society, 94(5), pp. 377-384 (1934). https://doi.org/10.1093/mnras/94.5.377.

[34] R. Danev and K. Nagayama. *Applicability of thin film phase plates in biological electron microscopy.* In: Biophysics, 2, pp. 35-43 (2006) doi: 10.2142/biophysics.2.35 https://doi.org/10.2142/biophysics.2.35.

[35] Y. Fukuda, Y. Fukazawa, R. Danev, et al. *Tuning of the Zernike phase-plate for visualization of detailed ultrastructure in complex biological specimens.* In: JOurnal of Structural Biology, 168, pp. 476-484 (2009). https://doi.org/10.1016/j.jsb.2009.08.011.

[36] R. Danev, H. Okawara, N. Usuda, et al. *A Novel Phase-contrast Transmission Electron Microscopy Producing High-contrast Topographic Images of Weak Objects.* In: Journal of Biological Physics, 28, pp. 627-635 (2002). https://doi.org/10.1023/A:1021234621466.

[37] R. Danev and K. Nagayama. *Complex Observation in Electron Microscopy: IV. Reconstruction of Complex Object Wave from Conventional and Half Plane Phase Plate Image Pair.* In: Journal of the Physical Society of Japan, 73(10), pp. 2718-2724 (2004). https://doi.org/10.1143/JPSJ.73.2718.

[38] M. Dries, S. Hettler, B. Gamma, et al. *A nanocrystallin eHilbert phase-plate for phase-contrast transmission electron microscopy.* In: Ultramicroscopy 139, pp. 29-37 (2014). http://dx.doi.org/10.1016/j.ultramic.2014.01.002.

[39] M. Malac, M. Beleggia, M. Kawasaki, P. Li et al. *Convenient contrastenhancementbyahole-freephaseplate.* In: Ultramicroscopy 118, pp.77-89 (2012). https://doi.org/10.1016/j.ultramic.2012.02.004.

[40] R. Danev, B. Buijsse, M. Khoshouei, et al. *Volta potential phase plate for in-focus phase contrast transmission electron microscopy.* In: PNAS, 111(44), pp. 15635–15640 (2014). https://doi.org/10.1073/pnas.1418377111.

[41] H. Boersch. *Über die Kontraste von Atomen im Elektronenmikroskop.* In: Zeitschrift für Naturforschung A, 2(11-12), pp. 615-633 (1947). https://doi.org/10.1515/zna-1947-11-1204.

[42] P.N.Y. Unwin. *An Electrostatic Phase Plate for the Electron Microscope.* In: Berichte der Bunsengesellschaft für physikalische Chemie, 74(11), pp. 1137-1141 (1970). https://doi.org/10.1002/bbpc.19700741110.

[43] P.N.Y. Unwin. *Electron microscopy of biological specimens by means of an electrostatic phase plate.* In: Proceedings of the Royal Society of London. Series A, Mathematical and Physical Sciences, 329, pp. 327-359 (1972). https://doi.org/10.1098/rspa.1972.0116.

[44] K. Schultheiss, F. Pérez-Willard, B. Barton, et al. *Fabrication of a Boersch phase plate for phase contrast imaging in a transmission electron microscope.* In: Review of Scientific Instruments, 77, 033701 (2006). https://doi.org/10.1063/1.2179411.

[45] J. Shiue, C.S. Chang, S.H. Huang, et al. *Phase TEM for biological imaging utilizing a Boersch electrostatic phase plate: theory and practice.* In: Journal of Electron Microscopy, 58(3), pp. 137-145 (2009). https://doi.org/10.1093/jmicro/dfp006.

[46] S.H. Huang, W.J. Wang, C.S. Chang. *The fabrication and application of Zernike electrostatic phase plate.* In: Journal of Electron Microscopy, 55(6), pp. 273-280 (2006). https://doi.org/10.1093/jmicro/dfl037.

[47] J. Zach. *Phase plate, Image producing method and Electron microscope.* World Intellectual Property Organization: 2008. Publication Number WO/2008/061603.

[48] S. Hettler, J. Wagner, M. Dries, et al. *On the role of inelastic scattering in phase-platet ransmission electron microscopy.* In: Ultramicroscopy 155, pp. 27-41 (2015). http://dx.doi.org/10.1016/j.ultramic.2015.04.001.

[49] K. Schultheiss, J. Zach, B. Gamm, et al. *New Electrostatic Phase Plate for Phase-Contrast Transmission Electron Microscopy and Its Application for Wave-Function Reconstruction.* In: Microscopy and Microanalysis, 16, pp. 785-794 (2010). https://doi.org/10.1017/S1431927610055042.

[50] R.R. Schröder, B. Barton, H. Rose and G. Benner. *Contrast Enhancement by Anamorphotic Phase Plates in an Aberration Corrected TEM.* In: Microscopy and Microanalysis, 13(S2), pp. 136-137 (2007). https://doi.org/10.1017/S143192760708004X.

[51] N. Frindt, K. Schultheiss, B. Gamm, et al. *The Way to an Ideal Matter-free Zernike and Hilbert TEM Phase Plate: Anamorphotic Design and First Experimental Verification in Isotropic Optics.* In: Microscopy and Microanalysis, 16(S2), pp. 518-519 (2010). https://doi.org/10.1017/S1431927610056436.

[52] Y. Aharonov and D. Bohm. *Significance of Electromagnetic Potentials in the Quantum Theory.* In: Physical Review, 115(3), pp. 485-491 (1959). https://doi.org/10.1103/PhysRev.115.485.

[53] C.J. Edgcombe. *A phase plate for transmission electron microscopy using the Aharonov-Bohm effect.* In: Journal of Physics: Conference Series, 241, 012005 (2010). https://doi.org/10.1088/1742-6596/241/1/012005.

[54] C.J. Edgcombe, A. Ionescu and J.C. Loudo. Characterisation of ferromagnetic rings for Zernike phase plates using the Aharonov–Bohm effect. In: Ultramicroscopy, 120, pp. 78-85 (2012). http://dx.doi.org/10.1016/j.ultramic.2012.06.011.

[55] C.J. Edgcombe, N. Dellby and O. Krivánek. *Evolution of Magnetic Ring Designs for Phase Plates.* In: Microscopy and Microanalysis, 21(S3), pp. 2299-2300 (2015). https://doi.org/10.1017/S1431927615012271.

[56] A.H. Tavabi, M. Beleggia, V. Migunov, et al. *Tunable Ampere phase plate for low dose imaging of biomolecular complexes.* In: Scientific Reports, 8, 5592 (2018). https://doi.org/10.1038/s41598-018-23100-3.

[57] Thermo Fisher Scientific Inc. *Glacios Cryo-TEM for Life Sciences.* [online, cited on 2022, May 19] https://www.thermofisher.com/cz/en/home/electron-microscopy/products/transmission-electron-microscopes/glacios-cryo-tem.html.

[58] JEOL Ltd. *CRYO ARM™ 300 (JEM-Z300FSC) Field Emission Cryo-Electron Microscope.* [online, cited on 2022, May 19] https://www.jeol.co.jp/en/products/detail/JEM-Z300FSC.html.

[59] D. Gabor. *Holography, 1948-1971.* In: Science, 177(4046), pp. 299-313 (1972). https://doi.org/10.1126/science.177.4046.299.

[60] P.W. Hawkes and J.C.H. Spence. *Handbookof Microscopy.* Springer, 2019. ISBN 978-3-030-00068-4.

[61] K. Yamamoto, Y. Sugawara, M.R. McCartney and D.J. Smith. *Phase-shifting electron holography for atomic image reconstruction.* In: Journal of Electron Microscopy, 59, pp. S81-S88 (2010). https://doi.org/10.1093/jmicro/dfq033.

[62] M. Duchamp, O. Girard, G. Pozzi, et al. *Fine electron biprism on a Si-on-insulator chip for off-axis electron holography.* In: Ultramicroscopy, 185, pp. 81-89 (2018). https://doi.org/10.1016/j.ultramic.2017.11.012.

[63] K. Ogai, Y. Kimura, R. Shimizu, et. al. *Microfabricated Submicron Al-Filament Biprism as Applied to Electron Holography.* In: Japanese Journal of Applied Physcis, 30(11B), pp. 3272-3276 (1991). https://doi.org/10.1143/JJAP.30.3272.

[64] G. Möllenstedt and H. Düker. *Beobachtungen und Messungen an Biprisma-Interferenzen mit Elektronenwellen.* In: Zeitschrift für Physik, 145, PP. 377-397 (1956). https://doi.org/10.1007/BF01326780.

[65] J. Faget and Ch. Fert. In: Comptes Rendus de l'Académie des Sciences, 243(2028), (1956).

[66] A. Ducharme, C. Johnson, P. Ercius and B. McMorran. *Optimized Amplitude-Dividing Beam Splitter Gratings for 4D STEM Holography.* In: Microscopy and Microanalysis, 27(S1), pp. 746-747 (2021). https://doi.org/10.1017/S1431927621003007.

[67] F.S. Yasin, T.R. Harvey, J.J. Chess, et al. *Probing Light Atoms at Subnanometer Resolution: Realization of Scanning Transmission Electron Microscope Holography.* In: Nano Letters, 18, pp. 7118-7123 (2018). https://doi.org/10.1021/acs.nanolett.8b03166.

[68] K.R. Hossain. *Transmission Electron Microscope [TEM].* In: 3D printing in your life (2014). [online, cited on 2022, May 19] https://3dprintinglife.wordpress.com/2021/12/04/transmission-electron-microscope-tem/.

[69] Pradeep Research Group. *High Resolution Transmission Electron Microscope (HRTEM) with EDAX.* [online, cited on 2022, May 19] https://pradeepresearch.org/microscopy-instruments/.

[70] Practical Electron Microscopy and Database. *Objective Lens in TEMs/STEMs.* [online, cited on 2022, May 19] https://www.globalsino.com/EM/page3765.html.

[71] M. Schmidt , F. Nazneen , P. Galvin, et al. *FIB Patterning of Stainless Steel for the Development of Nano-structured Stent Surfaces for Cardiovascular Applications.* In: FIB Nanostructures. Springer 2013, pp. 391-416. https://doi.org/10.1007/978-3-319-02874-3_16.

[72] Agar Scientific Ltd. *Silicon nitride membranes - 200um substrate thickness.* [online, cited on 2022, May 19] https://www.agarscientific.com/silicon-nitride-membranes-200-181-m-substrate-thickness.

[73] Agar Scientific Ltd. *Silicon dioxide films.* [online, cited on 2022, May 19] https://www.agarscientific.com/silicon-dioxide-films.

[74] Thermo Fisher Scientific Inc. *Helios 5 FX DualBeam Datasheet.* [online, cited on 2022, May 19] https://assets.thermofisher.com/TFS-Assets/MSD/Product-Information/helios-5-fx-semiconductor-datasheet-ds0283.pdf.

[75] SPI Supplies. *SPI Supplies Gold Crystal Specimen for Calibrating on Lattice Spacings.* [online, cited on 2022, May 19] https://www.2spi.com/item/02904-ab/.

[76] Agar Scientific Ltd. *Diffraction grating replicas.* [online, cited on 2022, May 19] https://www.agarscientific.com/diffraction-grating-replicas.

[77] Thermo Fisher Scientific Inc. *Talos F200C TEM.* [online, cited on 2022, May 19] https://www.thermofisher.com/cz/en/home/electron-microscopy/products/transmission-electron-microscopes/talos-f200c-tem.html.

[78] The abTEM code. *Contrast Transfer Function.* [online, cited on 2022, May 19] https://abtem.readthedocs.io/en/latest/walkthrough/05_contrast_transfer_function.html.

List of Abbreviations

BFP	back focal plane
C1	first condenser
C2	second condenser
CTF	contrast transfer function
FIB	focused ion beam
IP	image plane
O1	objective prefield
O2	objective postfield
PP	phase plate
SA	selected area
SEM	secondary electron microscope, secondary electron microscopy
SP	sample plane
TEM	transmission electron microscope, transmission electron microscopy

List of Supplementary Material

Python script including functions for numerical simulation of wave-optical elements.